Texas A&M University
Mechanical Engineering Department
Turbomachinery Laboratory
Tribology Group

A TEST RIG FOR EVALUATION OF FOIL THRUST BEARINGS: DYNAMIC STIFFNESS OF A METAL MESH THRUST FOIL BEARING

Research Progress Report to the TAMU Turbomachinery Research Consortium

TRC-B&C-02-2017

by

Travis Cable
Research Assistant

Luis San Andrés
Mast-Childs Chair Professor
Principal Investigator

May 2017

LARGE SIZE METAL MESH FOIL BEARINGS & TEST RIG FOR LOAD CAPACITY

TRC Project, TEES # 400124-00078

EXECUTIVE SUMMARY

Compact high speed turbomachinery, such as air cycle machines in passenger aircraft, use foil bearings (radial and thrust) since the early 1960's. Over the past several decades industry and government agencies have invested to further develop foil bearing technologies and their deployment in oil-free rotating machinery. Prominent to this date, bump-type foil bearings implement an underspring structure that provides resilience and material damping, both acting while the rotor is airborne in series with the stiffness and damping of a very thin gas film. Design and manufacturing of bump-type foil bearings is costly as it demands of extensive engineering and actual experience.

The report details the design and functionality of a test rig for evaluating the performance of air foil thrust bearings. In addition to the test rig, the report details the design and manufacturing of a novel Rayleigh-step metal mesh foil thrust bearing (MMFTB). This bearing consists of a solid bearing support, a number of circular Copper mesh sheets (wire diameter=0.25, 0.3 and 0.41 mm), and a steel top foil (0.127 mm thick) that makes six pads, each 45° in extent, and each with a photo-chemical etched step 0.019 mm in depth. Static load measurements show that a bearing made with either two sheets of metal mesh with 20 or 30 opening per inch (OPI) and a bearing made with three sheets of 40 OPI mesh display a nonlinear load vs. elastic deflection relation, similar to that of a bump foil thrust bearing in the archival literature.

Dynamic loads with frequency ranging from 40 Hz to 300 Hz apply on a stationary bearing (no shaft rotation) to produce a 5 μm small amplitude motion. The identified MMFTB axial stiffness is (mostly) constant and increasing with the applied static load. The equivalent damping from the mesh structure is hysteretic with an experimentally determined material loss factor ~ 0.2, largely unaffected by either the excitation frequency or the amplitude of applied load.

Similarly, (static) break-away torque measurements obtained in a bearing with a bare top foil and another with a foil coated with a Parylene N layer produce a significant sliding friction factor, ~ 0.35 and ~0.25, respectively. Both top foils show slight wear after the tests. More so the uncoated top foil which withstood the largest specific load, (just) 35 kPa.

With the bearing static performance quantified, metal mesh thrust bearings are ready for experiments with rotor speed.

TABLE OF CONTENTS

A TEST RIG FOR EVALUATION OF FOIL THRUST BEARINGS: DYNAMIC STIFFNESS OF A METAL MESH THRUST FOIL BEARING

Luis San Andrés and Travis Cable, May 2017

LIST OF TABLES

page

Table 1. Dimensions of a prototype Rayleigh step thrust foil bearing with a metal mesh substructure. 9

Table 2. Parameters for metal mesh substructures. Density of Copper, ρ_c = 8,960 kg/m^3 11

Table 3. Physical and thermal properties of Parylene N®, manufactured by Paracoat Technologies. 14

Table 4. Instrumentation on thrust bearing test rig. 20

Table 5. Rig capabilities. 21

Table 6. Coefficients of polynomials fitting recorded deflection and load data. 27

Table 7. Metal mesh thrust foil bearings: average stiffness and loss factor. Compare with data in [24]. .. 34

LIST OF FIGURES

page

Figure 1. Schematic views of (a) a tapered bump-type and (b) a Rayleigh step metal mesh thrust foil bearing. 8

Figure 2. (a) Assembled front view (b) an exploded view and (c) assembled back view of a Rayleigh step metal mesh thrust foil bearing. 9

Figure 3. Dimensional drawing of a single circular metal mesh layer for a metal mesh thrust foil bearing. 10

Figure 4. Photographs of several mesh substructures with various wire diameters and densities. (OPI: opening per inch) 11

Figure 5. Schematics and photographs of three six-pad Rayleigh-step top foils. 13

Figure 6. Isometric and cross-section views of a test rig for the evaluation of hydrodynamic foil thrust bearings. 15

Figure 7. Dimensional drawings of 4140 steel thrust collar for a gas bearing test rig (dimensions in inches). 16

Figure 8. Schematic views of load shaft for thrust bearing test rig. 17

Figure 9. Schematic views of an aerostatic load plenum for test rig. 18

Figure 10. (a) Photograph of air flow piping and (b) a cross-section view of aerostatic plenum and TB load shaft. 19

Figure 11. Setup for calibrating the aerostatic loading plenum. 22

Figure 12. Measured applied load versus chamber pressure ratio (P/P_a). 23

Figure 13. Photograph of a metal mesh thrust bearing installed on test rig. 24

Figure 14. Specific load (W/A) versus bearing displacement for bearings with up to three metal mesh sheets and with increasing mesh density (OPI varies). 25

Figure 15. Specific load versus bearing displacement for MMTBs (# sheets and OPI vary) and data for bump foil TB in Ref. [15]. 26

Figure 16. Schematic representation of the elastic compression process for a single mesh layer with a sinusoidal weave. 26

Figure 17. (a) Load and (b) Structural stiffness (K_s) versus bearing deflection for a metal mesh thrust bearing with one sheet and a bump type foil bearing from Ref. [15]. 28

Figure 18. A photograph of the thrust foil bearing test rig set up for dynamic analysis. 29

Figure 19. Axial dynamics model for test foil thrust bearing and load shaft. 29

Figure 20. MMFTB dynamic direct stiffness versus excitation frequency. Applied specific load W/A = 7.7, 19.7 and 32.9 kPa and three distinct mesh types. (amplitude Z= 0.005 mm) 31

Figure 21. MMFTB quadrature stiffness versus excitation frequency. Applied specific load *W*/*A* = 7.7, 19.7 and 32.9 kPa and three distinct mesh types. (amplitude Z= 0.005 mm) 32
Figure 22. MMFTB material loss factor versus excitation frequency for three applied specific loads of *W*/*A* = 7.7, 19.7 and 32.9 kPa and three different mesh types. (amplitude Z= 0.005 mm). 33
Figure 23. Average foil bearing stiffness and material loss factor versus applied specific load (*W*/*A*) for four thrust foil bearings.. 34
Figure 24. Depiction of drag torque measuring system with strain gauge load cell and a lever arm affixed to the load shaft. 35
Figure 25. Sliding friction factor vs. specific load for a MMFTB: coated top foil and uncoated top foil. . 36
Figure 26. Photographs of MMFTBs before and after break-away torque tests. 37

NOMENCLATURE

A	Area [m^2]
$\bar{A}$	Measured bearing absolute acceleration [m/s^2]
D	Diameter [m]
ΔE	Dissipated energy [J]
$\bar{F}$	Measured dynamic load [N]
f	Friction factor, $T/(W \cdot R_{mid})$ [-]
h	Hysteretic damping coefficient [N/m]
h_s, h_t	Step and taper heights [m]
i	Imaginary unit $\sqrt{-1}$
$\bar{K}$	Dimensionless stiffness, $K_{struct} w_d/(W/A)$ [-]
K	Linear stiffness coefficient [N/m]
MR	Mass ratio, $m_{mm}/(A_{mm} w_d \rho_c)$ [-]
m	Mass [kg]
N_{pad}	Number of bearing pads [-]
P, P_a	Pressure and ambient pressure [Pa]
R	Radius [m]
T	Torque [N.m]
t	Thickness [m]
w_d	Wire diameter [m]
$\bar{Z}$	Measured relative displacement between bearing and thrust collar [m]
z	Axial displacement
η	Material loss factor [-]
ρ	Density [kg/m^3]
$\Theta_L, \Theta_P, \Theta_S$	Land, pad and step arc extents [deg]
Ω	Rotor speed [rad/s]
ω	Excitation frequency [rad/s]

PROJECT GOALS, TASKS AND THEIR COMPLETION

TRC funds a three-year research program to bring the technology of metal mesh foil bearings (radial and thrust) to a commercialization level. The deployment of microturbomachinery (MTM) supported on metal mesh foil bearings (MMFBs) relies on overcoming intermittent contact and damaging wear during rotor start up and shut down as well as temporary rubs during normal operating conditions. Most importantly, however, is engineered thermal management, to ensure reliable performance in environments with large heat generation (as in permanent magnet motors). In the 3rd year of work with thrust and radial MMFBs, the continuation tasks are to:

(a) Refine test rig for the dynamic load characterization of metal mesh pads.

(b) Assemble a radial MMFB (5 pads), mount it atop a rotor, and measure its lift-off speed and break away torque, touchdown speed and stall torque, and drag power for tests with shaft speed to 40 krpm and an increasing static load (specific loads up to ~180 kPa, $W \leq 300$ lbf).

(c) Complete design and construct a novel metal mesh foil thrust bearing.

(d) Complete the construction and troubleshoot a test rig for evaluation of foil thrust bearings and perform static load tests with a metal mesh foil bearing.

For Task (a), refining the test rig for determining the dynamic performance of metal mesh pads, inclusion of a static load cell to the rig introduced additional degrees of freedom, making it difficult to characterize the system. After assembling the metal mesh bearing for testing on a dedicated test rig, experiments showed that the motor does not have the required torque to adequately characterize the performance of the large bearing. Once this was determined, no further experiments with the large diameter metal mesh bearing were attempted.

The majority of this report focuses on the progress made on Tasks (c) and (d), namely the design and manufacturing of a novel metal mesh thrust foil bearing and a test rig to characterize its performance. In addition to static load testing, the report shows experimental measurements of the dynamic axial force coefficients and break-away torque for a metal mesh thrust foil bearing.

BRIEF REVIEW OF PERTINENT LITERATURE

Hydrodynamic gas foil thrust bearings (FTBs) are self-acting mechanical devices for balancing thrust loads and maintaining the axial position of rotors in rotating machinery. Designers have employed compliant surface (foil) bearings (both radial and thrust) in small turbomachines since the early 1960s (air-cycle machines for example [1]), although their widespread use is limited by the lack of predictive tools for their performance as well as their relatively low load capacity (typically W/LD < 35 kPa) and small viscous damping, when compared to oil lubricated bearings [1]. Despite these limitations, a foil bearing subset bolsters a lesser part count and lack of regular maintenance when compared to their rigid geometry liquid lubricated counterparts. In addition, the compliant nature of the bearing top foil and substructure more readily accommodates mechanical imperfections such as runout on the runner surface. Foil bearings also operate well in extreme service environments (hot or cold temperature) and with increasing levels of contamination in the process fluid [1].

From the 1980s through the early 2000s, Heshmat *et. al* [2-5] published several analyses for compliant surface thrust foil bearings where individual bump strip layers support sector shaped thrust pads. The bump-type foil bearing (both radial and thrust) dominated the foil bearing literature through the 1990s, including the work of Iordanoff [6,7], culminating in several US Patents [8,9]. In the early 2000s, NASA Glen and Case Western University published open source data for bump-type TFBs with a single bump-foil layer (Generation I) to disseminate information on their capabilities and foster their wide spread use in industry [10-15]. To their credit, and the credit of researchers before them, the bump-type foil bearing (both radial and thrust) is readily used in industry [16-18], as the literature shows the bump-foil substructure to be reliable and well understood.

Despite the relatively widespread use of bump-type foil bearings, bump layers are expensive to manufacture and time intensive to design, thus leading to a constant search for low cost alternatives. Alkhateeb and Vance [19] first investigated the damping capability of compressed metal mesh “donuts” for use in aircraft engines. The metal mesh structure, commercially available at a low price, is easy to manufacture and also performs well at extreme temperatures [19]. Recently, San Andrés *et al.* incorporated a metal mesh as the underspring element in a foil journal bearing and show its performance is similar to (and even surpassing) that of a like-sized bump-type foil bearing.

This document describes the functionality of a test rig for thrust foil bearings as well as the design and manufacturing of a novel Rayleigh-step thrust bearing with six foil pads and a uniform metal mesh substructure. Experiments without rotor speed aim at characterizing the sliding friction coefficient and the underspring structure stiffness and loss factor.

A RAYLEIGH STEP THRUST FOIL BEARING SUPPORTED ON A METAL MESH SUBSTRUCTURE

In 1918 Lord Rayleigh performed the first analysis of a fixed geometry, infinitely long step bearing and determine an optimum step configuration that produces the largest load. Since 1918, researchers such as Archibald and Hamrock as well as Maday and others furthered the analysis of the Rayleigh step bearing. Hydrodynamic gas foil thrust bearings typically utilize a uniform circumferential taper to develop the lubricant wedge that generates a hydrodynamic pressure. Recently, Lee and Kim first analyze a bump-type Rayleigh step thrust foil bearing [23].

Figure 1 displays two thrust foil bearing configurations, one in which a bump foil underspring structure supports a circumferentially tapered foil, and the other where a metal mesh structure supports a Rayleigh step top foil.

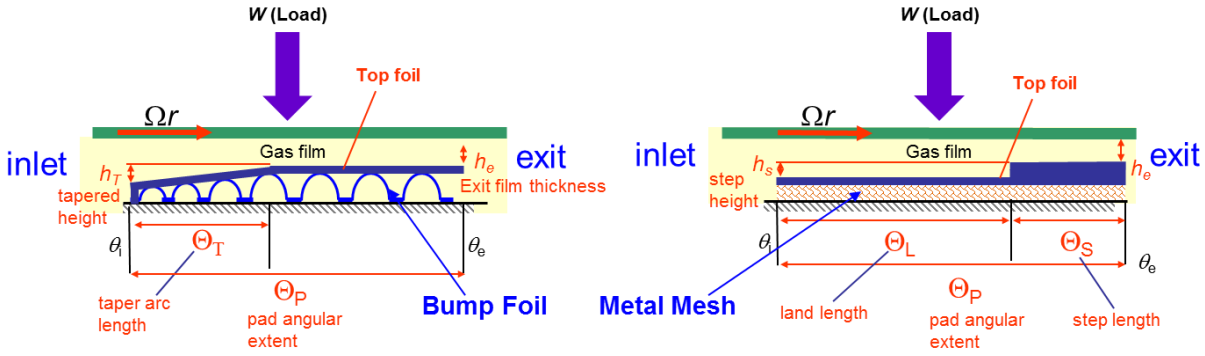

Figure 1. Schematic views of (a) a tapered bump-type and (b) a Rayleigh step metal mesh thrust foil bearing.

Figure 2 displays views of a prototype Rayleigh step thrust foil bearing consisting of three individual components, a solid metal bearing support, a thin circular metal mesh layer (or layers) and a thin metal Rayleigh step top foil.

Table 1 lists the geometry of each component (backing, mesh subsutructure and top foil). The bearing support is 316 stainless steel with a thickness of 9.53 mm. The support contains six small threaded holes (3-48 UNF) to fix both the circular mesh layers and Rayleigh step top foil; in addition, the support has six milled slots to provide cooling flow to the bearing pads. The copper metal mesh layers have outer diameters equal to that of the support, and inner diameters equal to that of the top foil. The 316 stainless steel Rayleigh step top foil consists of six sector shaped pads, each with circumferential extent of $\Theta_P = 45°$, and with inner and outer diameters of 50.8 mm and 101.6 mm, respectively. Each pad has a step etched into the metal to a depth of ~19 μm. The top foil thus has a piecewise thickness $t_{tf} = 0.108$ mm for $0 \le \theta < \Theta_L$ and $t_{tf} = 0.127$ mm for $\Theta_L \le \theta \le \Theta_P$ (as indicated in Figure 1 (b)).

Table 1. Dimensions of a prototype Rayleigh step thrust foil bearing with a metal mesh substructure.

	Bearing Support	Mesh Substructure
Material	316 Stainless Steel	Copper
Inner Diameter	45.72 [mm]	50.8 [mm]
Outer Diameter	120.65 [mm]	120.65 [mm]
Thickness	9.53 [mm]	~0.40 [mm]
	Rayleigh Step Top Foil	
Material	316 Stainless Steel	
Top Foil Thickness, t_{tf}	0.127 mm	
Step Depth, h_S	19.1 μm	
Coating	Parylene N	
Coating Thickness	3 μm	
Number of Pads, N_{PAD}	6 [-]	
Outer Pad Diameter, D_{PO}	101.6 mm	
Inner Pad Diameter, D_{PI}	50.8 mm	
Pad Arc Extent, Θ_P	45°	

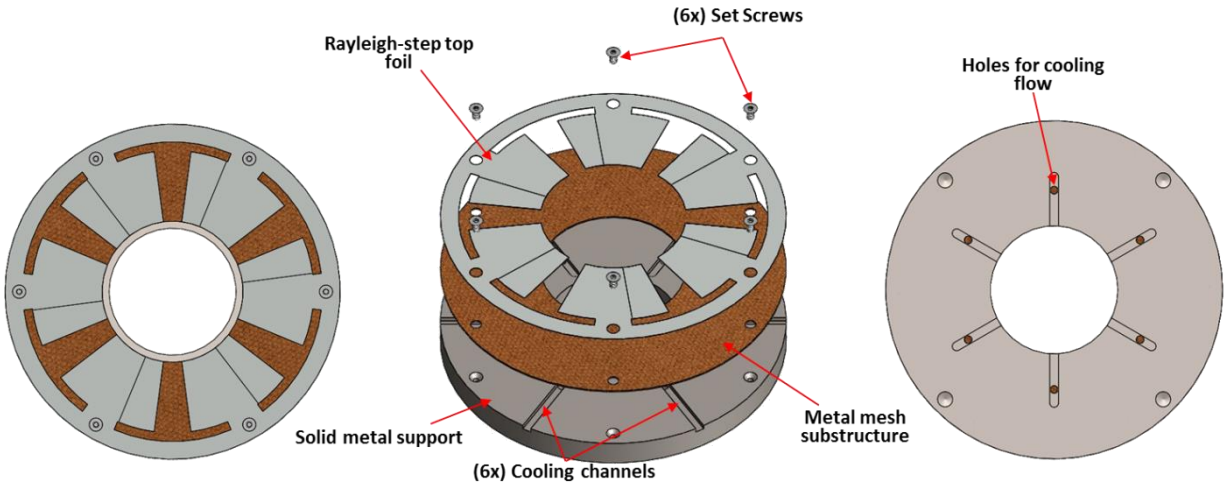

(a) Front View (b) Exploded View (c) Back View

Figure 2. (a) Assembled front view (b) an exploded view and (c) assembled back view of a Rayleigh step metal mesh thrust foil bearing.

MANUFACTURING METAL MESH LAYERS

Figure 3 displays a dimensional drawing (dimensions in inches) of a single metal mesh layer. The mesh manufacturer, TWP Inc., uses a laser cutting process to separate each circular mesh layer from a

sheet of uniform metal mesh. The six small holes on the 110.5 mm (4.35 in.) bolt circle as well as the 50.8 mm center hole are also laser cut, such that the diameters are nearly exact, and each of the mesh layers is nearly identical. Also of note, the copper mesh manufacturer produces metal mesh of uniform dimensions and with consistent weight per square foot, which is essential for uniformity.

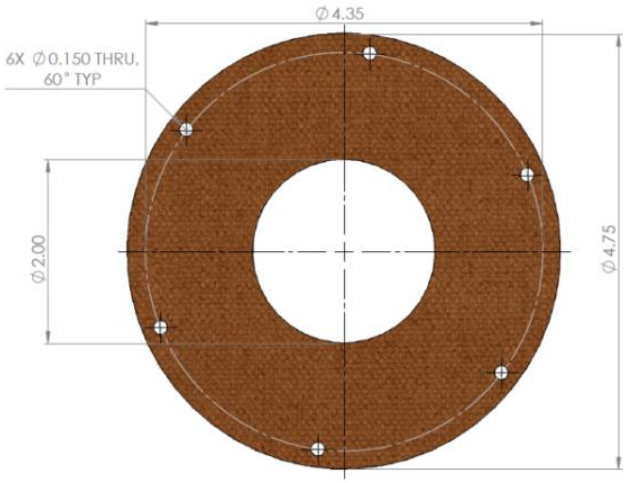

Figure 3. Dimensional drawing of a single circular metal mesh layer for a metal mesh thrust foil bearing.

Figure 4 displays a photograph showing three distinct mesh substructures. The metal meshes have different wire diameters (w_d) and are classified by the manufacturer in "openings per inch" (OPI). From the left to the right, in Figure 4, the meshes are 20, 30 and 40 OPI, respectively. Unlike a radial metal mesh bearing, the layers for a MMTFB sit on top of one another, and are not compressed into a single solid. However, a mass ratio can be construed for a MMTFB, considering the ratio of the mass of a single mesh layer to that of the layer if it was solid copper. A mass ratio follows as

$$MR = \frac{m_{MM}}{A_{MM} w_d \rho_c} \tag{1}$$

where m_{MM} is the measured mass of a mesh layer, A_{MM} is its area, w_d is the wire diameter (or height) and ρ_c is density of copper.

(a) 20 OPI (b) 30 OPI (c) 40 OPI

Figure 4. Photographs of several mesh substructures with various wire diameters and densities. (OPI: opening per inch)

Table 2 summarizes the mesh parameters for each mesh type. The mass ratio MR = 0.44, 0.51 and 0.59 for the 20, 30 and 40 OPI meshes, respectively. Note that more OPI results in a finer mesh and a higher mass ratio. Metal mesh journal bearings typically utilize mesh structures with mass (or compactness) ratios greater than 0.25. For the current experiments, TWP provided ten sheets of each configuration, for a total of 30 mesh sheets. Each mesh is weighed on a precise digital scale (±0.01 g) prior to use.

Table 2. Parameters for metal mesh substructures. Density of Copper, ρ_c = 8,960 kg/m^3. (OPI: opening per inch)

	20 OPI	**30 OPI**	**40 OPI**
Wire Diameter, w_d [mm]	0.406	0.305	0.254
Square Opening Size [mm]	0.864	0.533	0.381
Measured Mass per Circular Sheet, m_{MM} [g]	15.00 (±0.10)	13.00 (±0.10)	12.55 (±0.10)
Circular Sheet Area, A_{MM} [cm^2]	93.4	93.4	93.4
Mass Ratio, MR [-]	0.44	0.51	0.59

MANUFACTURING A RAYLEIGH STEP TOP FOIL

As mentioned earlier, the Rayleigh step top foil is 316 stainless steel and has six arcuate pads, each containing a small Rayleigh step. For rigid geometry step bearings, the steps are typically machined into the bearing surface via traditional means, such as milling. Manufacturing multiple small (less than 25.4 μm) steps into a thin (~0.127 mm thick) metal sheet requires of a non-conventional method. Photochemical milling (or etching) exposes metal to UV light through engineered phototools with predesigned images. Areas on the sheet with no laminate are eroded when exposed to the UV light, forming the intended shapes of the foil. A second photoetch develops the steps in each of the foils by exposing the intended areas to UV light over a shorter duration, eroding only some of the metal. This process produces extremely uniform steps on all of the foils.

Figure 5 displays three Rayleigh step top foils, each with pad inner and outer diameters of 50.8mm and 101.6mm, respectively. The foils are each 0.127mm thick and have a thin (5.08mm) circular band connecting the six pads at the foil outer diameter. Six small fixture holes, located on a 110.5 mm (4.35 in.) bolt circle, provide locations to fix the top foil to the mesh substructure and the solid metal backing.

Figure 5 (a) shows a top foil where a 19 μm step occurs 15° from the pad leading edge, and Figure 5 (b) shows a pad where the step occurs 22.5° from the leading edge. The schematic in Figure 5 (c) depicts a new concept, a “negative slant” Rayleigh step configuration, where the step starts at the outer diameter of the pad at the leading edge, and finishes at the inner diameter at the pad trailing edge. The orientation of the negative slant intendeds to oppose the centrifugal pumping effect that typically forces lubricating fluid out of the hydrodynamic loading zone. For the experiments herein, three prototypes are manufactured for each configuration, for a total of nine test top foils.

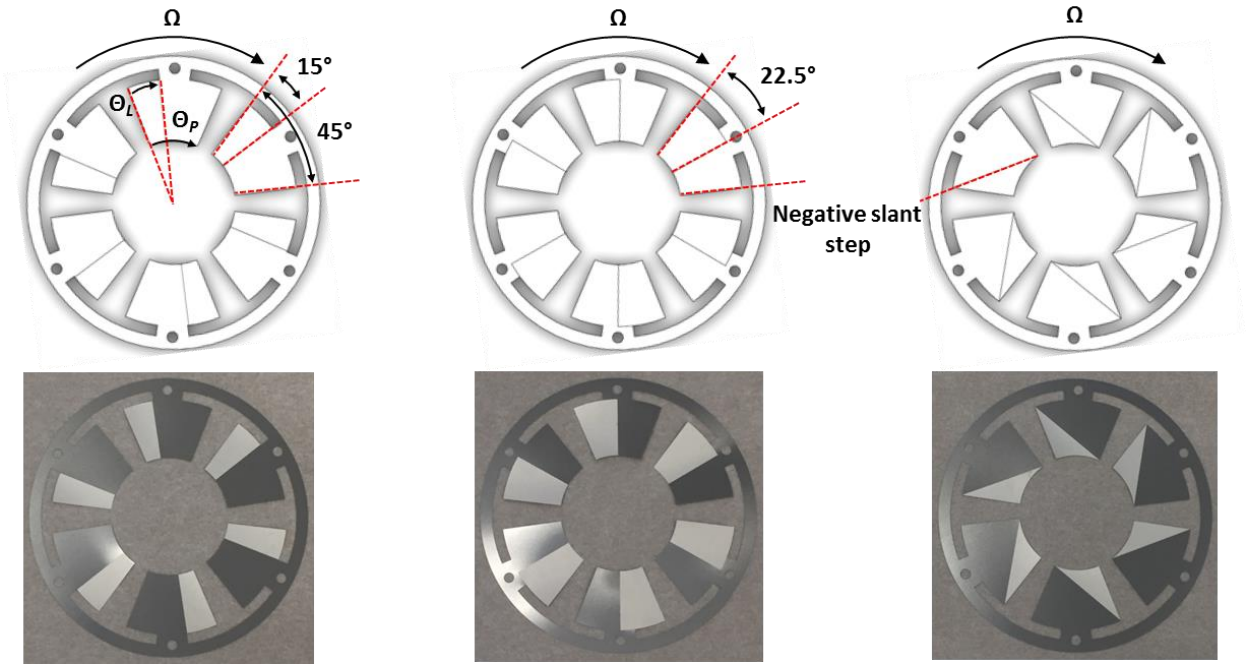

(a) Step location $\Theta_L/\ \Theta_P = 1/3$ (b) Step location $\Theta_L/\ \Theta_P = 1/2$ (c) Negative Slant, $0 \leq \Theta_L \leq 45°$

Figure 5. Schematics and photographs of three six-pad Rayleigh-step top foils.

During startup and shutdown, foil bearings experience solid contact between the rotor and top foil, and thus are in need of enduring coatings to reduce wear. The Rayleigh step top foil necessitates a coating that is robust, yet thin enough as to not interfere with the step height (19 μm). Traditional foil bearings implement MoS_2, PTFE or a NASA designed PS304® coating to reduce the coefficient of friction between the top foil and the runner. As MoS_2 and PTFE require coating thicknesses of at least 25.4 μm, and the NASA PS304® coating requires a run-in process at a high (~300° C) temperature, the Rayleigh step top foil requires a different coating. To reduce the coefficient of friction between the foils and the thrust runner, the thrust runner has a 25.4 μm thick layer of thin dense chrome and the top foils have a thin (~3 μm) Parylene N® coating [Table 3 lists some properties for the coating]. The Parylene coating, manufactured by Paracoat Technologies, is deposited via a vapor deposition process, yielding a coating which is uniform, conformal, flexible and robust. The uses of Parylene range from o-rings to medical implants to electrical components. Note that the three top foils in Figure 5 are not coated, while the other two sets of foils have the Parylene coating.

Table 3. Physical and thermal properties of Parylene N®, manufactured by Paracoat Technologies.

	Magnitude
Yield Strength	2.4 GPa
Density	1.11 g/cm^3
Static Coefficient of Friction	0.25
Dynamic Coefficient of Friction	0.25
Melting Temperature	410 °C
Thermal Conductivity	0.12 W/m.K

A TEST RIG FOR THE EVALUATION OF HYDRODYNAMIC FOIL THRUST BEARINGS

Gas thrust bearing test rigs [5, 10, 22, 24] typically measure bearing load capacity, drag torque, bearing temperature rise and axial force coefficients. Most test rigs share a similar design, consisting of a floating load shaft and a thrust runner which is spun by either an electric motor or an impulse turbine. An aerostatic bearing (or bearings) typically levitates the load shaft, on which the test bearing resides, allowing the bearing to rotate and translate axially without friction.

Figure 6 displays a photograph and a cross-section view of a test rig for characterizing the static and dynamic forced performance of gas hydrodynamic thrust foil bearings. The test rig consists of four main components, a solid steel thrust collar spun by a 2.2 kW router motor (40 krpm max), a thrust load shaft, an aerostatic loading plenum, and a test bearing. As depicted in Figure 6, the aerostatic plenum contains two porous carbon bushings which float the load shaft, on which the test bearing fixes via threaded connections. The following sections detail each of the test rig components as well as instrumentation and operating capabilities.

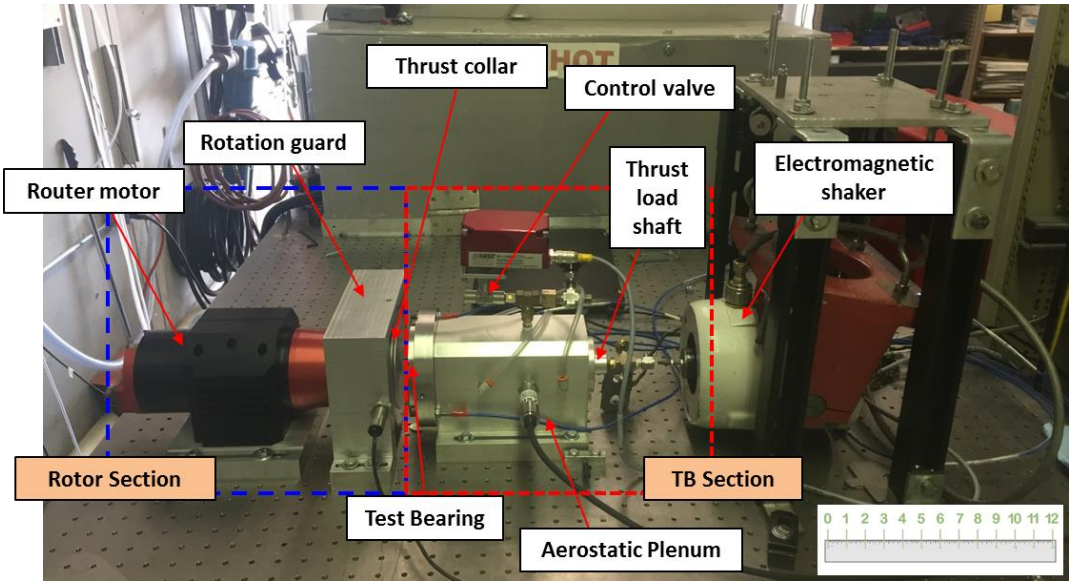

(a) Isometric View

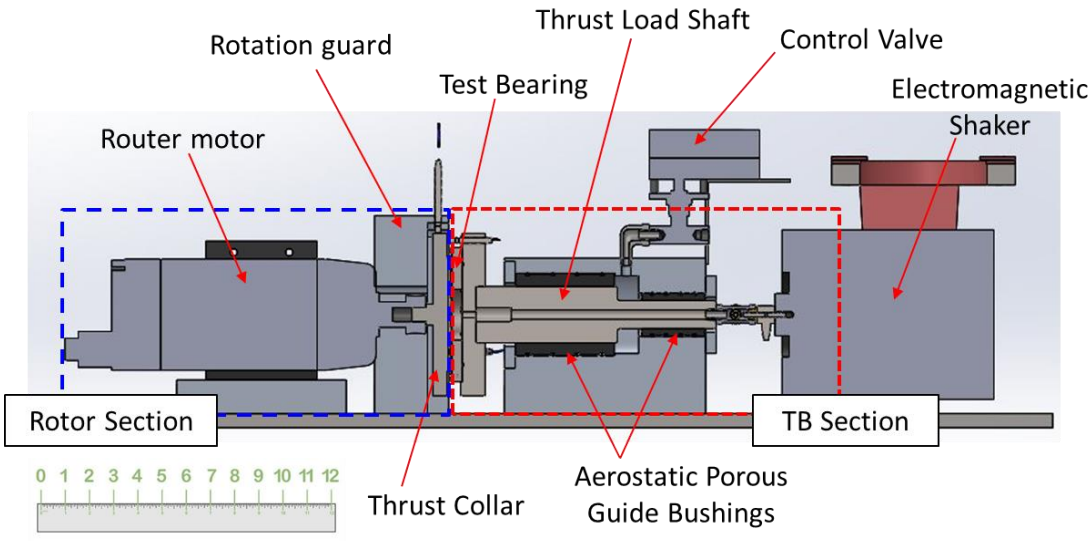

(b) Cross-section view

Figure 6. Isometric and cross-section views of a test rig for the evaluation of hydrodynamic foil thrust bearings.

The section on the left side of the schematic in Figure 6 (b), labeled "Rotor Section", consists of a metal disk (collar) fixed in a router motor via a collet and precision nut. Figure 7 displays dimensional drawings of the 4140 steel thrust collar, having an outer diameter of 146mm (5.75 in.). The front face of the thrust collar has a stepped area with a diameter of 102.1mm (4.02 in.) and a 25.4 μm layer of thin dense chrome. A test bearing mates against this stepped area to develop hydrodynamic pressure. The

recessed ridge, from 102.1mm to 146mm, provides a location for three non-contacting displacement sensors to measure the relative displacement between the thrust runner and a test bearing. As machined, the measurement surface has ~25 µm of mechanical runout, while the stepped ridge has less than 15 µm. The collar is precision balanced and has a residual imbalance of 0.014 g-cm.

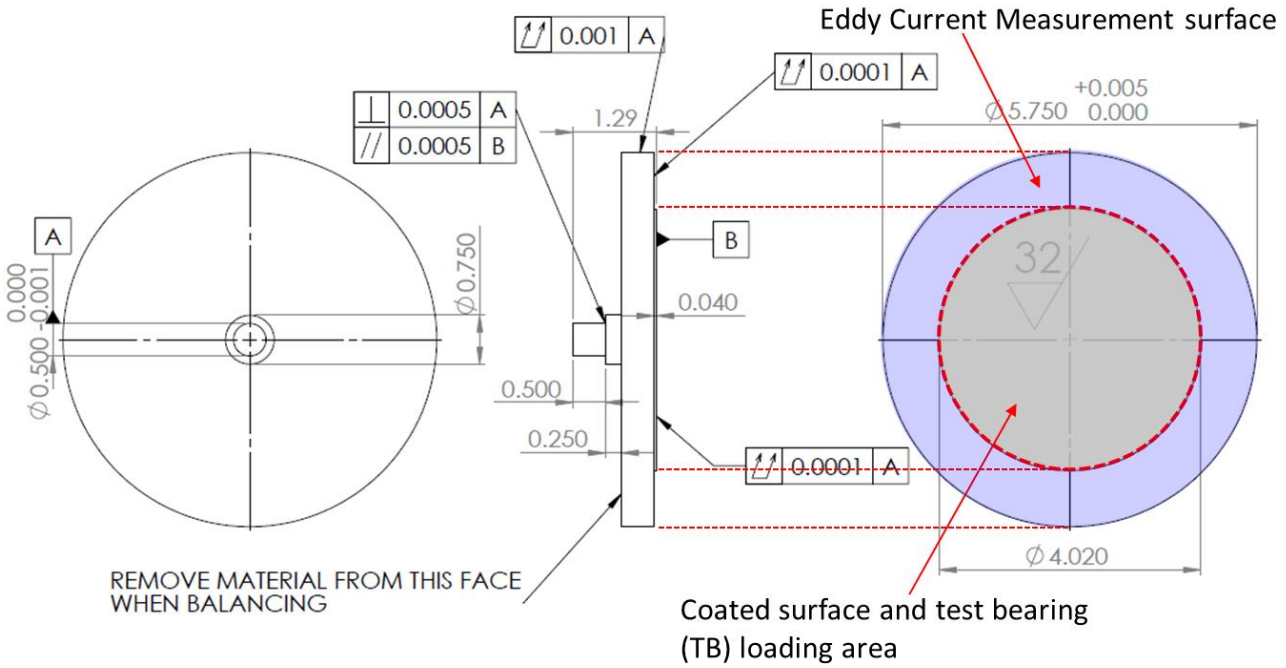

(a) Back View (b) Side View (c) Front View

Figure 7. Dimensional drawings of 4140 steel thrust collar for a gas bearing test rig (dimensions in inches).

The right portion of the test rig, labeled TB Section in Figure 6, consists of an aerostatic plenum with two porous guide bushings, a load shaft and a test bearing. Figure 8 displays both isometric and exploded views of the load shaft and attached test bearing, indicating the individual components. The cylindrical bushing shaft is 21.6 cm long and has diameters slightly smaller than the porous carbon guide bushings (25.4 and 50.8 mm, respectively). Although not pictured in Figure 8, a small diameter thru hole locates at the center of the load shaft, allowing cooling flow to the test bearing. The step at the center of the bushing shaft provides an area (A_{SL} ~ 14.7 cm^2) for the chamber pressure (described in more detail below) to create a static load, pushing the test bearing into the thrust runner.

A circular 316 stainless steel loading flange bolts onto the bushing shaft and holds the test bearing as well as three eddy current sensors. At the back end of the bushing shaft, an 1/8th" NPT connection allows

for the application of cooling flow as well as providing attachments for a dynamic load cell and a torque arm for determining the bearing drag torque. Finally, an o-ring, placed between the test bearing and loading flange, ensures that the entirety of the supplied cooling flow reaches the test bearing.

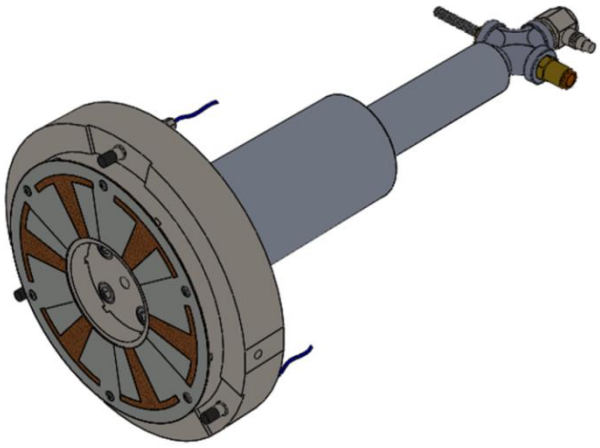

(a) Isometric view

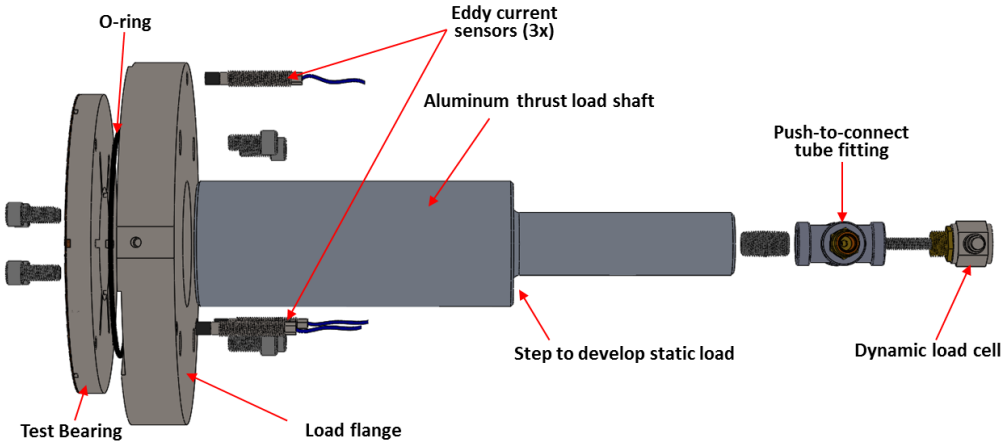

(b) Exploded view of a thrust load shaft with individual components labeled

Figure 8. Schematic views of load shaft for thrust bearing test rig.

Figure 9 displays an isometric view and an exploded view of the aerostatic plenum, indicating the individual components. Pressurized air, up to 7.9 bara (115 psia), supplies two hydrostatic porous graphite bushings[1] through two push-to-connect fittings threaded into the plenum body. Some of the flow through the bushings escapes to ambient, while some travels to the central cavity, increasing its static pressure. The porous graphite bushings float the shaft on a small (~ 4 μm) air film and also act as seals for the central cavity due to their extremely tight radial clearance. A high precision (+/- 0.08%) static

[1] Porous bushings manufactured and supplied by New Way Air Bearings.

pressure transducer measures the pressure in the central chamber, while a precise motor actuated control valve (CV = 0.03) sets the pressure in the center chamber to achieve a desired static load on the test bearing. The resulting static load on the test bearing is approximately $F \approx \Delta P A_{SL}$, where A_{SL} = 14.7 cm^2. A cross-section view of the plenum and load shaft, shown in the next figure, helps to illustrate this concept.

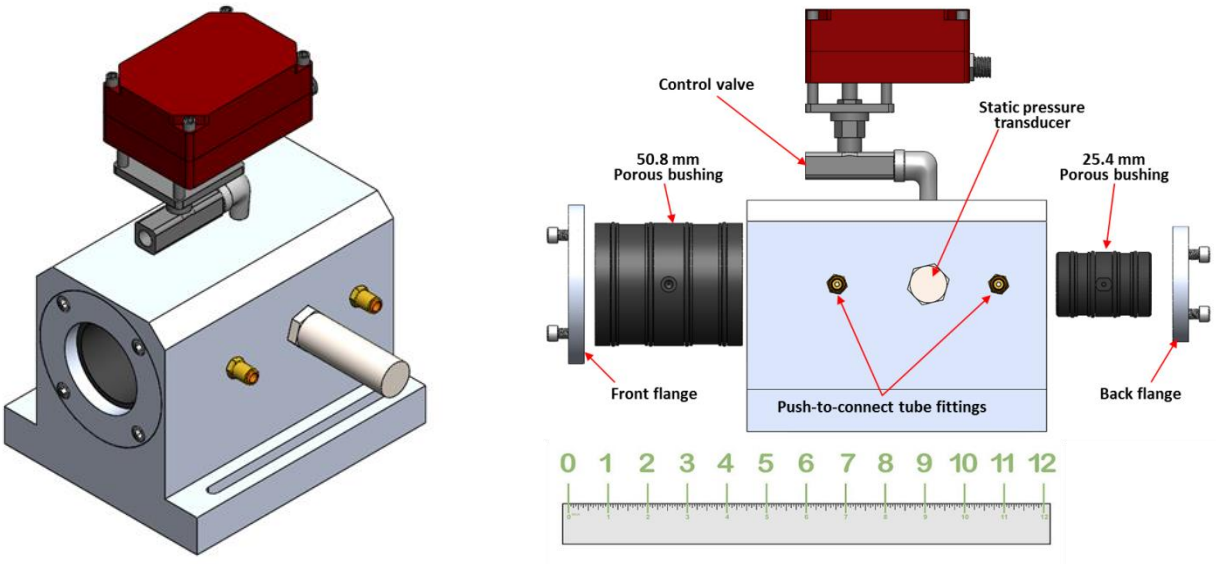

(a) Isometric view (b) Exploded view with individual components labeled

Figure 9. Schematic views of an aerostatic load plenum for test rig.

In addition to the supply flow to the bushings, a thru hole along the shafts center allows for compressed air to cool a test bearing. A precision needle valve (CV = 0.47) controls the cooling flow to the bearing while a mass flow meter measures the flow (max of 500 SLPM). Figure 10 shows the piping for the supply flow and cooling flow as well as a schematic cross-section view of the TB load shaft assembled in the aerostatic plenum, indicating the directions of the supply and cooling flows as well as the resulting static load from the pressure in the center chamber.

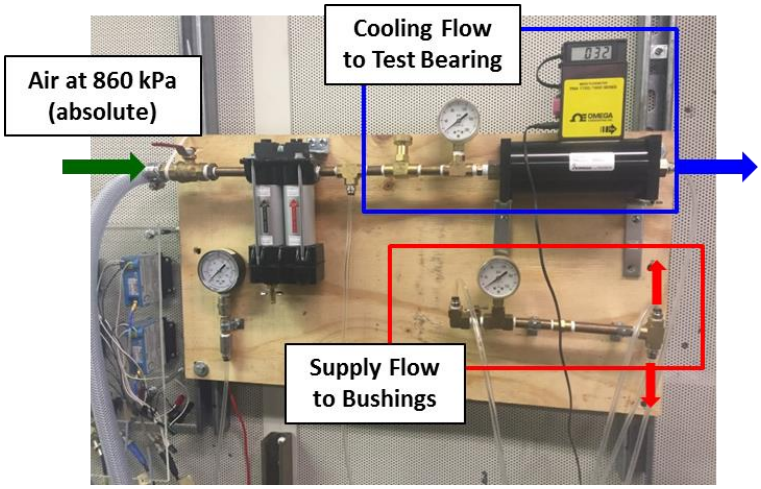

(a) Flow loop for supply and cooling flow

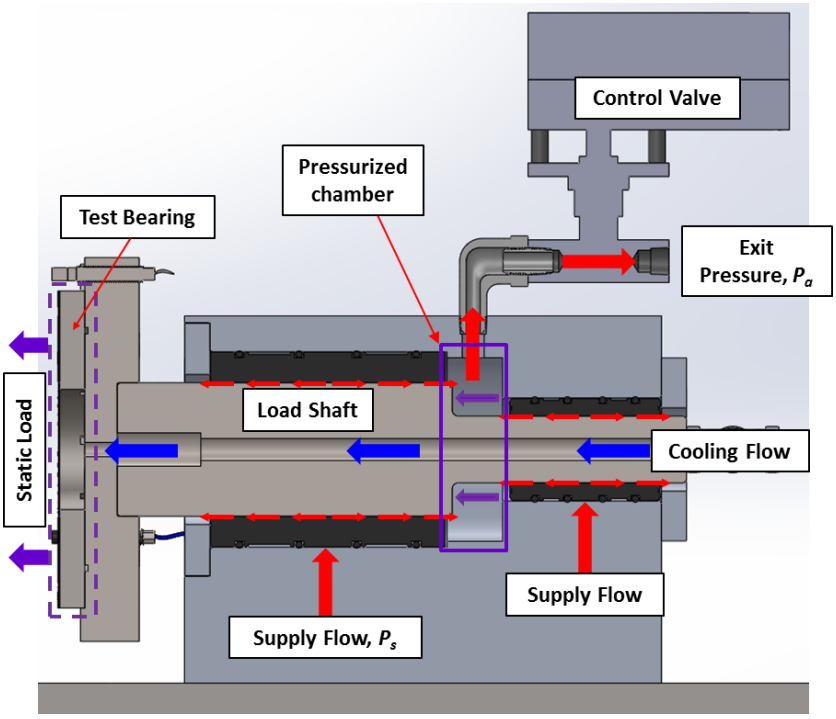

(b) Cross-section of aerostatic plenum with load shaft installed

Figure 10. (a) Photograph of air flow piping and (b) a cross-section view of aerostatic plenum and TB load shaft.

Table 4 lists the instrumentation on the test rig as well as the quantities they measure and their associated uncertainties. In total, the rig has 5 eddy current sensors, 4 thermocouples, a static pressure

transducer, a static load cell, an infrared tachometer, dynamic load cell, and an accelerometer. All of the data is recorded using commercial data acquisition (DAQ) software and in-house LabVIEW® programs.

Table 4. Instrumentation on thrust bearing test rig.

	Quantity	Cost	Measurement	Uncertainty
Eddy Current Sensor	5	$4,700	Thrust runner radial vibration and test bearing relative axial displacement	± 0. 3% of probe distance
Thermocouple	4	$200	Test bearing and motor temperatures	±2.2 °C or 0.75% of measurement
Mass Flow Meter	1	$1,200	Cooling flow rate	± 5 SLPM
Static Pressure Transducer	1	$500	Chamber pressure	± 0. 08 psia
Static Load Cell	1	$450	Bearing drag torque	0.26 N
Dynamic Load Cell	1	$415	Test bearing dynamic load	± 1 N
Accelerometer	1	$380	Test bearing absolute acceleration	≤ 0.5 m^2/s
Infrared Tachometer	1	$210	Thrust runner rotational speed	±10 rpm
Valve Controller	1	$1,600	Valve position	2°
		$9,655	Instrumentation cost	

Table 5 lists the capabilities for the thrust foil bearing test rig. The router has two sets of angular contact ball bearings, with a total static axial load capacity of 1.4 kN. The motor-torque curve from the manufacturer indicates that the 2.2 kW motor can deliver torque up to 1.1 N.m. In short, the rig can apply static loads up to 580 N (W/A ~ 127 kPa (18.4 psi) for the current bearing), and dynamic loads up to 100 N via an electromagnetic shaker whilst spinning the thrust collar to a max speed of 40 krpm ($R_{PO}\Omega$ = 212 m/s). The thru hole in the TB load shaft facilitates cooling flow to the test bearing with a range from 0 – 500 SLPM. The load flange on the load shaft can accept foil thrust bearings with outer diameters (ODs) equal to 101.6mm. At the bearing outer diameter the surface speed of the thrust runner is ~212 m/s.

With a test thrust bearing in place, the rig allows the measurement of bearing drag torque, pad temperatures, static load versus deflection behavior, dynamic axial force coefficients and load capacity. All of these measurements can also be performed with increasing amounts of cooling flow.

In addition to the instrumentation on the rig, a National Instruments DAQ hardware consists of a CDAQ-9174 chassis and four analog output/input modules: 9205 (±10 V analog input module), 9263 (±10 V analog output module), 9234 (±5 V sound and vibration input module), and 9211 (±80 mV temperature input module). The DAQ hardware totals **~$4,500.**

The manufacturing for the rig components (thrust collar, rotation guard, motor base, load shaft, load flange, bearing support and plenum) cost ~$10,000, while the additional balancing and coating of the thrust collar adds $2,300. Adding the costs of instrumentation, DAQ hardware, and test rig components, totals **~$26,500.**

Table 5. Rig capabilities.

Operating Speed, $R_{PO}\Omega$	0 – 40 krpm (212 m/s)
Motor Torque Capability	1.1 N.m
Bearing OD Limit	101.6 mm
Static Load	0 - 580 N
Dynamic Load	0 – 100 N
Cooling Flow	0 – 500 SLPM

PERFORMANCE OF A (STATIONARY) METAL MESH THRUST FOIL BEARING

The prototype foil thrust bearing, pictured in Figure 2, has dimensions (inner and outer diameter, number of pads and pad arc extent) identical to those of a bump foil TB in the archival literature [13-15,24]. Stahl [15] gives comprehensive data on the static load performance (load versus deflection) as well as the operating characteristics (drag torque and load capacity) of this bump foil TB, while Balducchi *et al.* [24] detail the dynamic forced performance (stiffness and damping) of another bump foil TB with identical dimensions. The rest of this document compares the test data for the novel metal mesh thrust foil bearing to those for the bump foil TBs in Refs. [15,24] to assess the effectiveness of the metal mesh design.

Prior to operation, the aerostatic plenum (see Figure 9) is calibrated with a strain gauge load cell in order to determine the static load applied to a test bearing. Figure 11 displays the test setup for correlating the pressure in the plenum to the applied static (push) load. A strain gauge load cell attaches to the center of the loading shaft and pushes up against the steel thrust runner. Shop air at 517 kPa (absolute) supplies to the porous guide bushings, while the control valve starts in the open position (small load on the shaft). Note that when the valve is fully open, and the bushings are supplied with 517 kPa (absolute) air, the

plenum (absolute) pressure ratio is P/P_a = 1.25. Although not desirable to have pressure in the plenum with the valve fully open, the plenum necessitates a very small orifice valve to precisely control the chamber pressure.

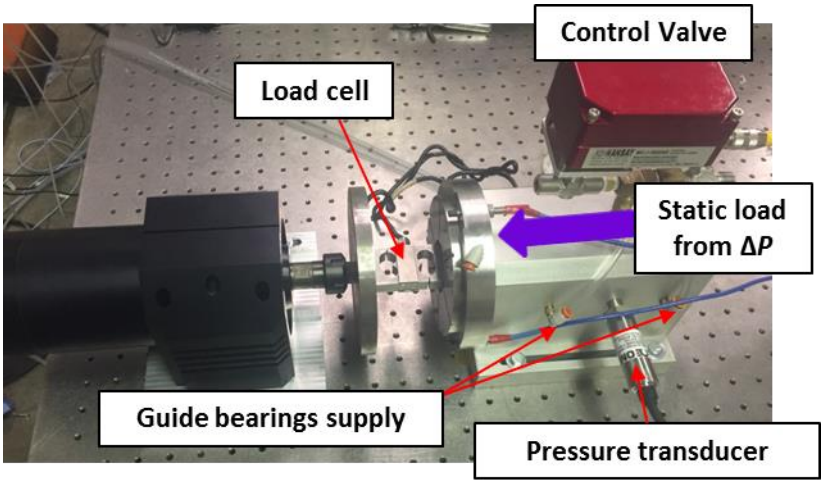

Figure 11. Setup for calibrating the aerostatic loading plenum.

With the rig set up as pictured in Figure 9, the control valve moves to a fully closed position while the DAQ software records the static load and the pressure in the central chamber. Figure 12 displays the measured force from the static load cell versus the pressure in the central chamber when the electromagnetic shaker is attached to the load shaft and when it is not attached. In addition to the measured force, Figure 12 displays a line fit for the static load on the shaft, $W = P \cdot A_{LS}$, where P is the chamber (gauge) pressure and A_{LS} is the shaft area (~14.7 cm^2).

The results in Figure 12 show that the measured static load diverges from the simple approximation when the plenum pressure ratio reaches P/P_a ~2.5 (150 kPa), but it is linear over the valve's full opening range, from fully open to fully closed. A linear fit of the load vs. pressure data determines the effective loading area ($F = PA_{effective}$) to be $A_{effective}$ = 14.2 cm^2, compared to the actual loading area of A_{LS} = 14.7 cm^2. The calibration also shows that the plenum load vs pressure behavior is identical with and without the shaker attached to the load shaft, indicating that the stiffness of the shaker armature (K_{shaker} = 12.3 kN/m) will neither load nor unload (statically) the test bearing during dynamic tests.

After reaching the maximum pressure (P/P_a ~ 3.25), the valve opens again, and the plenum chamber pressure decreases. Figure 12 shows that there is an amount of hysteresis present during the de-pressurization of the plenum. This hysteresis is due to the pressure force acting along a single direction (i.e. pushing the load shaft into the thrust runner). As the plenum depressurizes, there is no force pulling the load shaft back, but rather, the pre-compressed strain gauge load cell elongates again when the

chamber pressure decreases to a certain magnitude. This delay (i.e. hysteresis) depends on the maximum pressure in the plenum as well as how fast the valve opens, and it is not currently quantified.

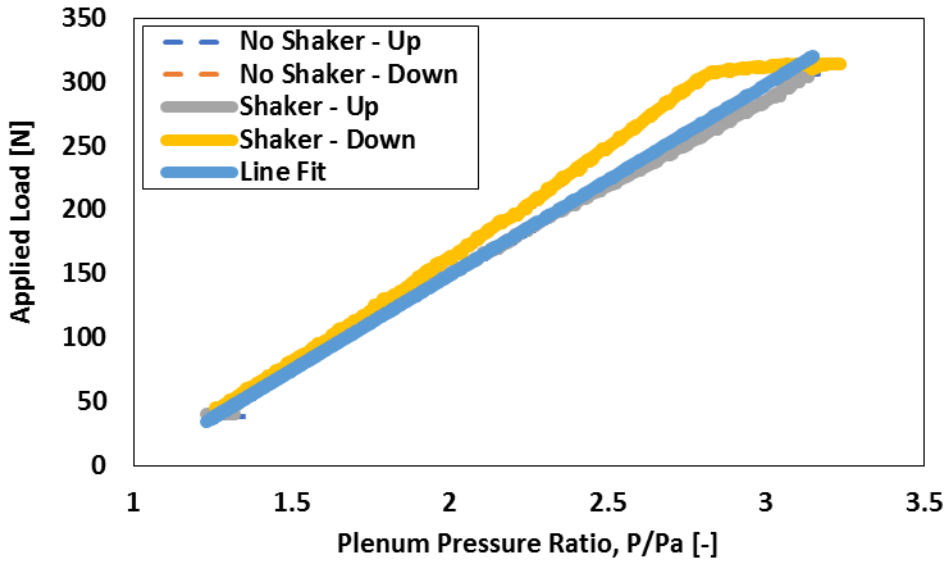

Figure 12. Measured applied load versus chamber pressure ratio (P/P_a).

Figure 13 depicts the metal mesh foil thrust bearing installed on the test rig from Figure 6. Three eddy current sensors locate on the outer diameter of a loading flange (labeled in Figure 13) on which the test thrust bearing mounts. The three sensors, located on a diameter of ~143 mm and spaced 120° apart, record the relative displacement between the test bearing and the thrust runner. Before conducting the load versus deflection tests, the test bearing mounts to the load shaft, but has no foil or mesh layers in place (solid metal bearing support only). A static load (up to W/A = 34 kPa) pushes the thrust bearing support into the thrust collar, while the DAQ records the relative displacements of the three eddy current sensors. Alignment between the two surfaces is adjusted by shimming the plenum and repositioning it until the relative displacements between the sensors and the runner are within 5 μm of each other at the maximum applied load.

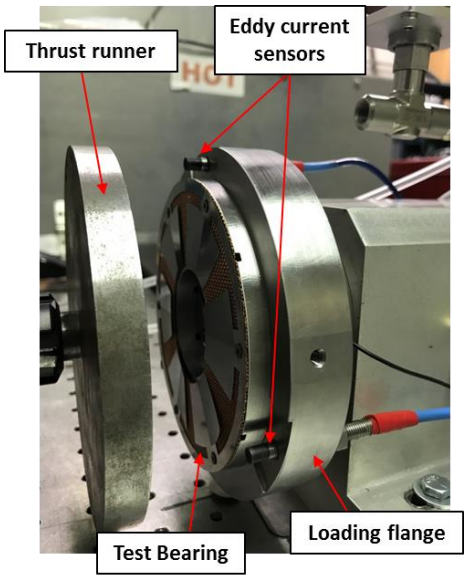

Figure 13. Photograph of a metal mesh thrust bearing installed on test rig.

STATIC LOAD VERSUS DEFLECTION FOR A METAL MESH THRUST FOIL BEARING

The goal of the current research is to compare the performance of the MMFTB to that of a similar size BFTB in the literature [13-15,24]. To compare the performance between two foil bearings, it is desirable for the MMTFB to have a structural stiffness (stiffness of the metal mesh underspring structure) similar to that of the BFTB. The number of mesh layers for the assembled bearing depends on the application. Conventional wisdom indicates that a MMFTB with more layers has a smaller structural stiffness than a MMTFB with fewer layers (the layers act as springs in series). In addition, the MMTFB with more layers should have a larger material damping (more wire connections allow for more energy dissipation through sliding friction).

Figure 14 displays static specific load (*W/A*) versus bearing deflection for the MMFTB having 1, 2 or 3 layers and with mesh sizes of 20, 30 and 40 OPI. The deflections displayed in Figure 14 are the average displacement of the three eddy current sensors, thus representing the axial translations of the bearing center. In addition, each of the curves is an average of three load cycles. Note that the bearings are preloaded with 30 N *(W/A*~10 kPa) before the tests begin to avoid an area where a small force causes a large displacement (as present in Ref. [27]). Figure 14 displays only the load cycles, and not the unload data, due to the uncharacterized pressure hysteresis from the air pressurized plenum.

Figure 14 (a) shows that the MMFTBs with a single sheet are very stiff, with deflections less than, or equal to, 25 μm for loads up to 70 kPa. Increasing the number of mesh layers softens the bearing, thus producing a larger deflection amplitude. In general, using sheets with a finer mesh (higher mass ratio,

MR) creates a stiffer bearing. Essentially, a looser mesh weave and a larger wire size allow for more movement of the individual wires.

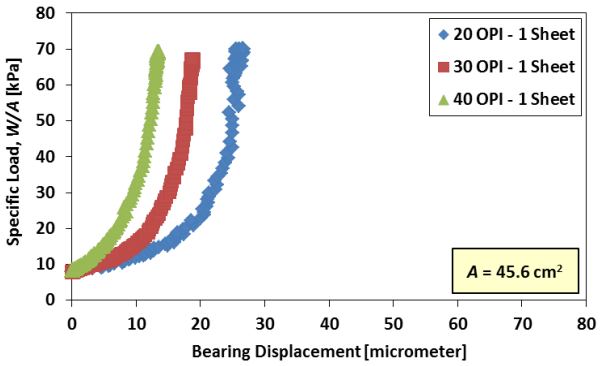

(a) Bearing with 1 metal mesh sheet

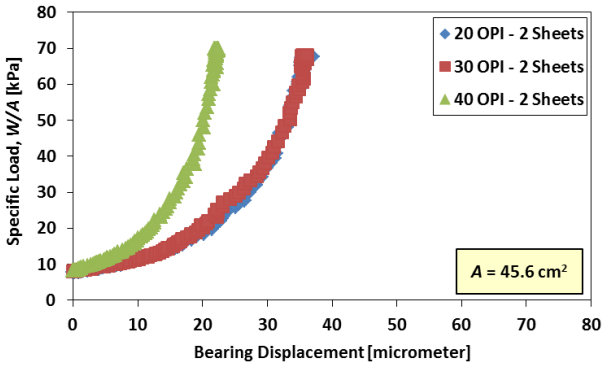

(b) Bearing with 2 metal mesh sheets

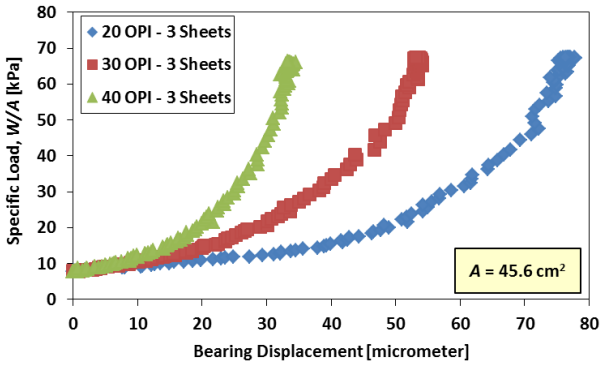

(c) Bearing with 3 metal mesh sheets

Figure 14. Specific load (*W*/*A*) versus bearing displacement for bearings with up to three metal mesh sheets and with increasing mesh density (OPI varies).

Figure 15 displays the static specific load (*W*/*A*) versus deflection results from Stahl [15] as well as three of the MMTFBs (from Figure 14) with similar deflection behavior. The test data shows the typical hardening nonlinearity common to foil bearings. The illustration in Figure 16 lends physical insight into this hardening nonlinearity, for a single sheet of interwoven mesh wires. In its undeformed state, the mesh layer is not entirely flat, but the wires intertwine in a sinusoidal-like pattern, one over another. When a static load applies to the structure, the mesh wires elongate, losing their curvature and forming a flat layer of mesh. Intuitively, this suggests that mesh layers with larger wires and a lesser OPI (i.e. more room to expand) should be more flexible, as confirmed by the results in Figure 14.

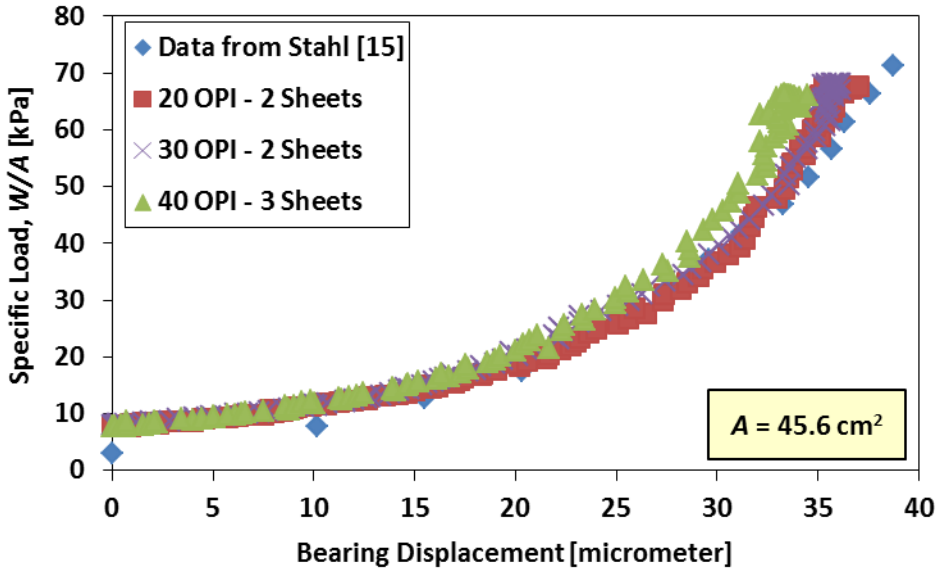

Figure 15. Specific load versus bearing displacement for MMTBs (# sheets and OPI vary) and data for bump foil TB in Ref. [15].

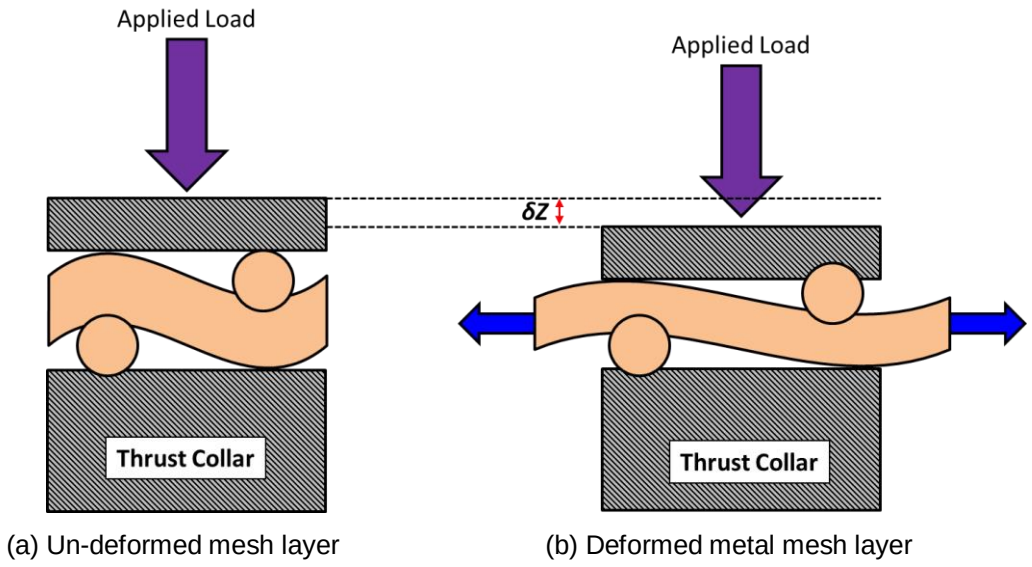

Figure 16. Schematic representation of the elastic compression process for a single mesh layer with a sinusoidal weave.

An odd order polynomial models the pad reaction force *W(x)* as a function of the mesh deflection (*x*). Presently,

$$W(x) = K_1 x + K_2 x^2 + K_3 x^3 + W_0 \tag{2}$$

is quite adequate to fit the test data with a good correlation coefficient (R^2>=0.99). Table 6 lists the coefficients for the polynomials.

Table 6. Coefficients of polynomials fitting recorded deflection and load data.

	Load W (N) vs displacement x (μm) $W(x) = K_1 x + K_2 x^2 + K_3 x^3 + W_0$			
Bearing	K_1 [N/μm]	K_2 [N/μm^2]	K_3 [N/μm^3]	R^2
20 OPI – 2 Sheets	4.03	-0.307	0.011	0.99
30 OPI – 2 Sheets	3.52	-0.235	0.100	0.99
40 OPI – 3 Sheets	3.48	-0.259	0.011	0.99
Stahl [15]	2.97	0.098	0.006	0.99

The bearing structural stiffness K_s is derived from

$$K_s = \frac{dW}{dx} = K_1 + 2K_2 x + 3K_3 x^2 \tag{3}$$

A non-dimensional stiffness can be construed using the specific load and mesh wire diameter (w_d). For consistency, the wire diameter for the 20 OPI mesh (w_d = 0.4 mm) non-dimensionalizes the results.

$$\bar{K} = \frac{K_s w_d}{(W / A)} \tag{4}$$

Figure 17 displays the stiffness ($\bar{K}$) versus deflection for the four bearings in Figure 15. All of the bearings start with a large stiffness (smallest load) which then decreases and finally flattens out for increasing deflection (and load). This behavior indicates that the under-spring metal mesh structure is nonlinear, moving first through a regime where a small increase in load causes a large displacement (i.e. small stiffness), then to a region where the stiffness and load increase proportionally, resulting in a relatively constant $\bar{K}$. Quantitatively, the four bearings start relatively soft (K_s < 5 MN/m), but become quite stiff after ~25 μm (1 mil) of displacement and have a structural stiffness approaching 25 MN/m.

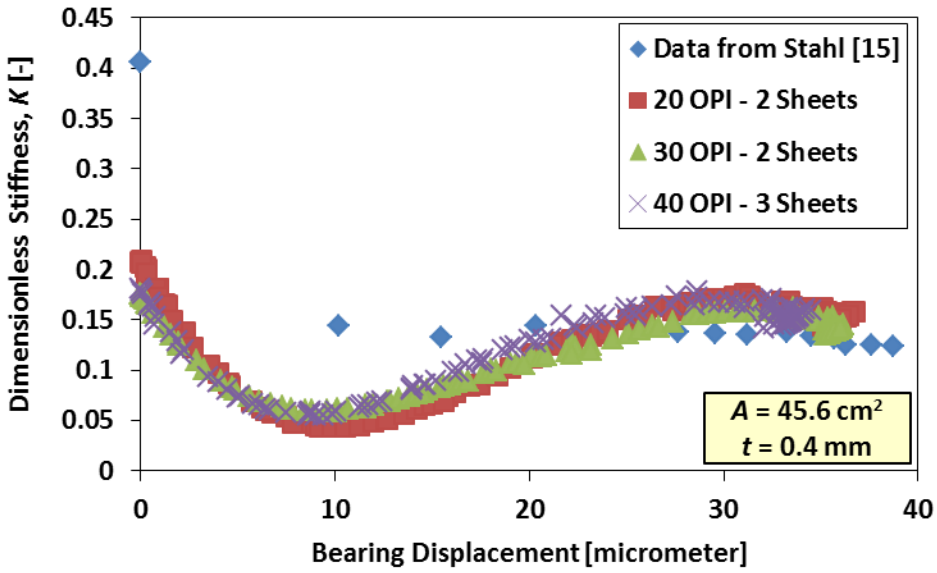

Figure 17. (a) Load and (b) Structural stiffness (K_s) versus bearing deflection for a metal mesh thrust bearing with one sheet and a bump type foil bearing from Ref. [15].

DYNAMIC STIFFNESS OF A METAL MESH TRHUST FOIL BEARING

During operation with a foil bearing, the structural stiffness and material damping of the underspring (metal mesh or bump foils) acts in series with the stiffness and damping of the air film. Hence, characterizing the dynamic performance of the underspring structure is necessary. Balducchi *et al.* [24] perform experiments to determine the stiffness and equivalent viscous damping for a BFTB with dimensions identical to those of the current MMTFB. In Ref. [24], Balducchi *et al.* use a pseudo-random waveform as outlined by Burrows *et al.* [25] to obtain a 5 μm dynamic bearing displacement for a frequency range comprised between 150-750 Hz and for five applied static loads (30-150 N, in 30 N increments).

Figure 18 displays a photograph of the test rig set up for dynamic load measurements. An electromagnetic shaker connects to the back of the static load shaft and imposes a dynamic load on the test bearing. The aerostatic guide bushings (3.8 μm radial gap) allow for friction free motion, and as such, contribute negligible stiffness and damping (in the axial direction) to the test system. A high precision (1 V/g) single axis accelerometer, mounted on the backside of the loading flange, records the absolute acceleration of the test bearing while the three eddy current sensors record the relative displacement between the test bearing and the thrust collar.

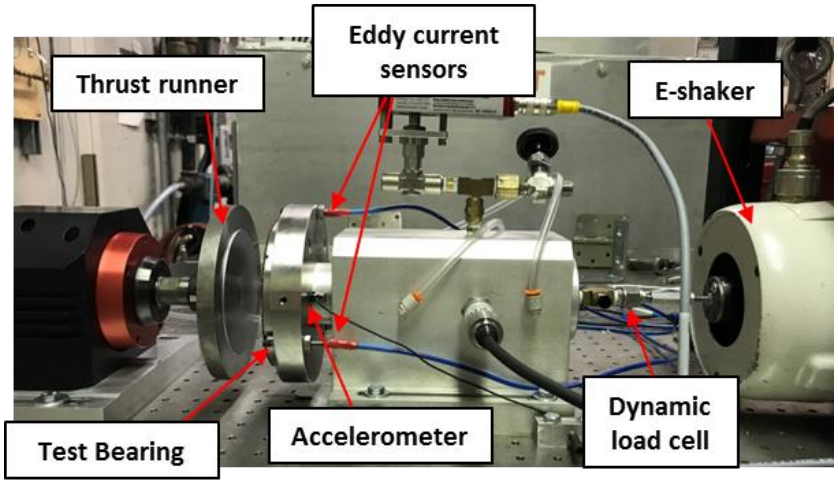

Figure 18. A photograph of the thrust foil bearing test rig set up for dynamic analysis.

Figure 19 displays a dynamics model of the test system. In the figure, m_1 = 4.22 kg refers to the mass of the load shaft and test bearing assembly, while m_2 is the mass of the thrust collar and the router motor armature (unknown total mass). The aerostatic plenum applies a static load (W_0) to the test bearing while the shaker imposes a periodic dynamic load (F) to the back of the load shaft, where a dynamic load cell resides.

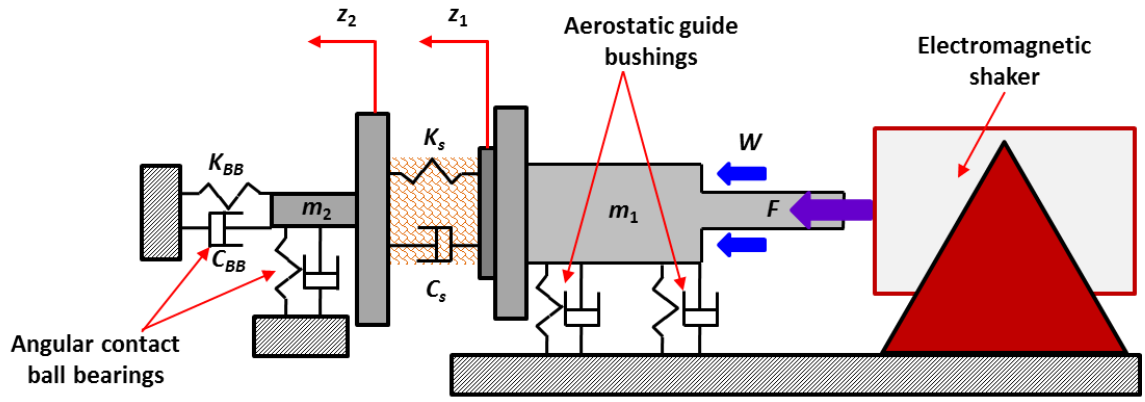

Figure 19. Axial dynamics model for test foil thrust bearing and load shaft.

The equation of motion (EOM) for the load shaft and MMTB in Figure 19 is

$$m_1\ddot{z}_1 = F(t) - F_{MMFTB} \tag{5}$$

Consider a periodic excitation force ($\bar{F}$) superimposed on a static load (W_0). The ensuing periodic displacements have the same frequency, i.e.

$$F(t) = \bar{F}\, e^{i\omega t} + W_0 \rightarrow z(t) = \bar{Z}\, e^{i\omega t} + z_0 \tag{6}$$

where ω is the excitation frequency, $\bar{F}$ is the dynamic force applied to the end of the load shaft and $\bar{Z}$ is the (averaged) relative displacement between the thrust runner and the eddy current sensors. The resulting EOM in the frequency domain is

$$\left(\bar{F} - m_1 \bar{A}\right) = \bar{F}_{MMFTB} \tag{7}$$

where $\bar{A}$ is the measured absolute acceleration of the test bearing and $\bar{F}_{MMFTB}$ is the dynamic reaction force of the test bearing. The real and imaginary parts of the bearing complex stiffness determine the dynamic stiffness and damping coefficients,

$$\frac{\left(\bar{F} - m_1 \bar{A}\right)}{\bar{Z}} = \frac{\bar{F}_{MMTFB}}{\bar{Z}} \rightarrow H \sim \left(K + i\omega C\right) \tag{8}$$

As mentioned, the goal of the current analysis is to compare the performance of the MMTFB to that of a similar BFTB, thus, it is desirable to reproduce both the dynamic displacement amplitude (5 μm) and frequency range of excitations (150-750 Hz) for the same applied loads 30-150 N (in 30 N increments), as in Ref. [24]. However, the shaker can only deliver ~100 N dynamic loads. Due to the limited power from the shaker, the frequency range for the current tests limits to excitations with frequency 40 Hz to 300 Hz and with a dynamic displacement amplitude $|Z|$ of 5 μm.

For expediency, this section presents dynamic stiffnesses for three MMFTBs (bearing with 3 sheets of either 20, 30, or 40 OPI mesh) and for three applied static loads (W/A =7.7, 19.7, and 32.9 kPa). The shaker applies a single frequency periodic load to the test bearing, in 20 Hz increments, while the DAQ records the dynamic load, acceleration, and relative displacements between the eddy current sensors and the thrust collar. The sampling rate is 10,240 samples/s. Each data point in the following plots is an average of 5 s of elapsed data (i.e. 51,200 samples). In addition, error bars for each of the following data sets represent the uncertainty in the measurements, determined with a student *t* distribution and a 95% confidence interval.

Figures 20 and 21 display the real and imaginary parts of the MMFTB dynamic stiffness (H) for three applied static loads W/A = 7.7, 19.7 and 32.9 kPa. The average dynamic displacement amplitude is 5 μm. The results in Figure 20 show that the real part of $H \rightarrow$ direct stiffness K is constant over the whole frequency range, indifferent to either the load or the type of mesh (20, 30, or 40 OPI). K magnitude increases with an increase in applied static load and also with the mass ratio of the mesh. The imaginary part of H (quadrature stiffness) increases with both the applied load and mesh mass ratio, and also with the excitation frequency.

Note that while each data set does have associated error bars, as mentioned earlier, the variation between the cycles is so small that the error bars do not extend past the data markers.

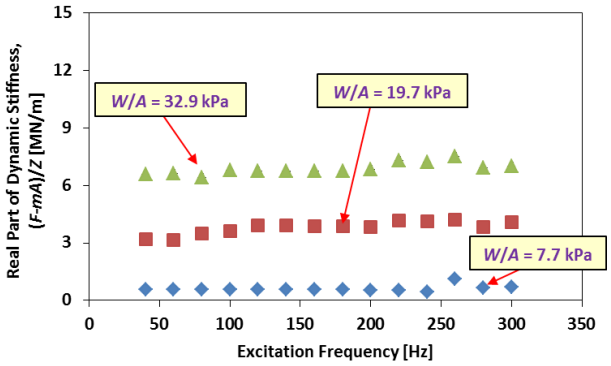

(a) Bearing with 3 Sheets of 20 OPI Metal Mesh

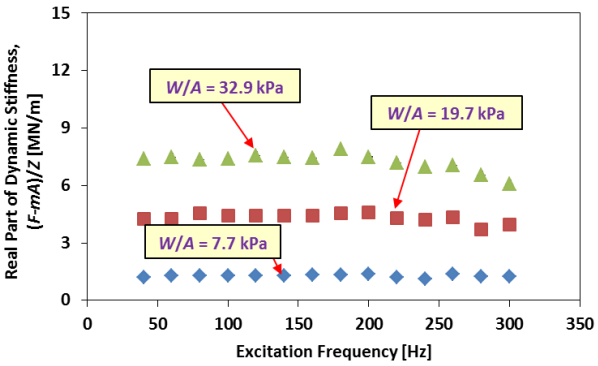

(b) Bearing with 3 Sheets of 30 OPI Metal Mesh

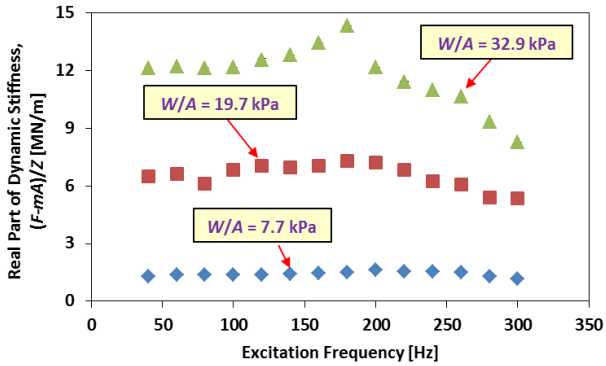

(c) Bearing with 3 Sheets of 40 OPI Metal Mesh

Figure 20. MMFTB dynamic direct stiffness versus excitation frequency. Applied specific load *W/A* = 7.7, 19.7 and 32.9 kPa and three distinct mesh types. (amplitude Z= 0.005 mm)

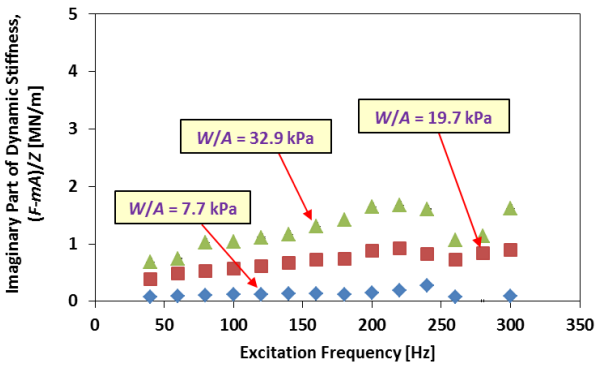

(a) Bearing with 3 Sheets of 20 OPI Metal Mesh

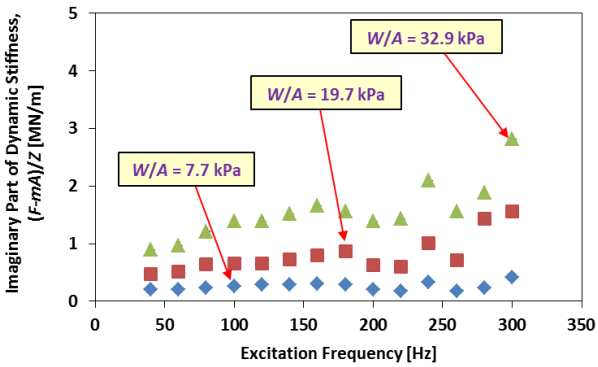

(b) Bearing with 3 Sheets of 30 OPI Metal Mesh

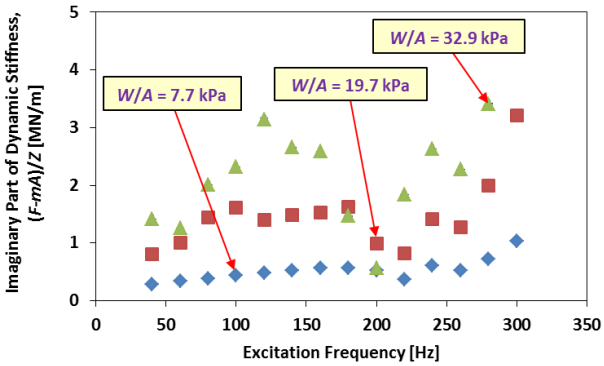

(c) Bearing with 3 Sheets of 40 OPI Metal Mesh

Figure 21. MMFTB quadrature stiffness versus excitation frequency. Applied specific load *W/A* = 7.7, 19.7 and 32.9 kPa and three distinct mesh types. (amplitude Z= 0.005 mm)

Damping in metal mesh structures is best quantified by a combination of viscous, hysteretic and dry-friction behaviors [20]. However, Alkhateeb [20] and Chirathadam and San Andrés [19,21] show that modeling energy dissipation in a mesh structure as purely material damping is adequate. The energy dissipated in a single period by a material with hysteretic damping is

$$\Delta E_{hys} = -\pi K \gamma Z^2 \tag{8}$$

where γ is a material loss factor. Assuming the metal mesh is characterized as

$$\bar{F}_{MMFTB} = K\left(1+i\,\gamma\right)\bar{Z} \tag{9}$$

Then, the loss factor follows from the measured complex stiffness (H) as

$$\gamma = \frac{\mathrm{Im}\left\{H_{(\omega)}\right\}}{\mathrm{Re}\left\{H_{(\omega)}\right\}} \tag{10}$$

Figure 22 displays the bearing MM material loss factor (γ) for three MMFTBs subjected to static load W/A = 7.7, 19.7 and 32.9 kPa. For the bearing with 20 and 30 OPI mesh sheets, γ~0.18 is largely unaffected by either the applied load or the excitation frequency, 40-300 Hz. For the MMFTB with 40 OPI mesh sheets, the average γ decreases slightly with an applied load (from γ = 0.35 for W/A = 7.7 kPa to γ = 0.21 for W/A = 32.9 kPa).

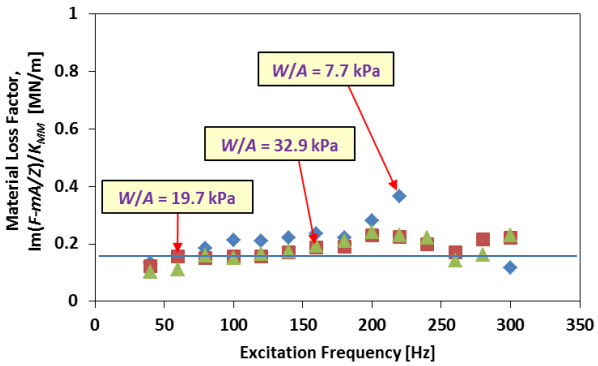

(a) Bearing with 3 Sheets of 20 OPI Metal Mesh

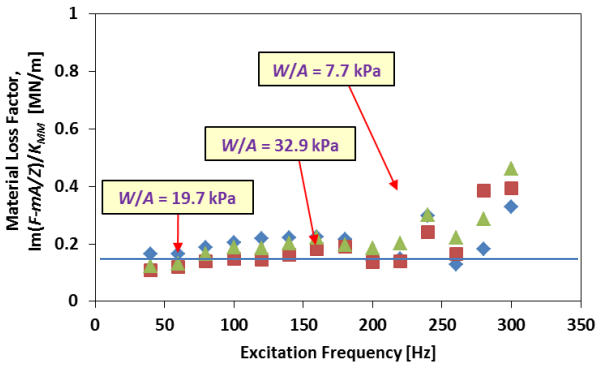

(b) Bearing with 3 Sheets of 30 OPI Metal Mesh

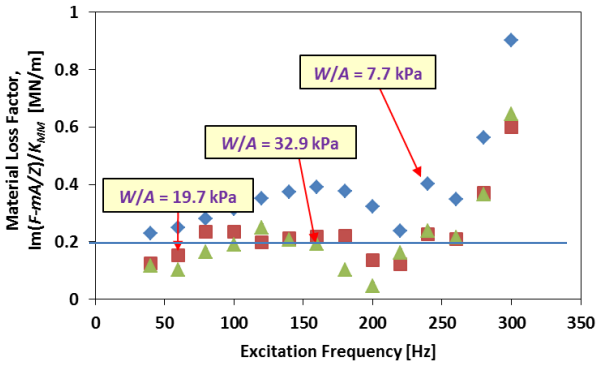

(c) Bearing with 3 Sheets of 40 OPI Metal Mesh

Figure 22. MMFTB material loss factor versus excitation frequency for three applied specific loads of W/A = 7.7, 19.7 and 32.9 kPa and three different mesh types. $\bar{Z}$ = 5 μm.

Table 6 and Figure 23 summarize the MMFTB stiffness and loss factor for the three distinct mesh types and for an increasing specific load. The excitation frequency range is 40-300 Hz. Table 6 also includes data for an average loss factor and average stiffness coefficient for the BFTB in Ref. [24]. The data from Baladucchi is a best representation, as the authors don't list average magnitudes for bearing stiffness or loss factor.

The data in Table 6, as well as the graphical representation in Figure 23, show that the MMFTB has a similar dynamic structural performance as that for the BFTB in Ref. [24]. The MMFTB that is the most similar to the BFTB from Ref. [24] is a metal mesh bearing with three sheets of OPI 40 mesh.

Table 7. Metal mesh thrust foil bearings: average stiffness and loss factor. Compared with data in [24].

	20 OPI Mesh		30 OPI Mesh		40 OPI Mesh		BFTB from Ref. [24]	
Specific Load (*W/A*) [kPa]	***K*** **[MN/m]**	γ **[-]**	***K*** **[MN/m]**	γ **[-]**	***K*** **[MN/m]**	γ **[-]**	K_{BF} **[MN/m]**	γ_{BF} **[-]**
7.7	0.61	0.21	1.27	0.20	1.41	0.38	2.5	~0.1
19.7	3.81	0.18	4.32	0.19	6.55	0.23	7.5	~0..35
32.9	6.87	0.18	7.23	0.22	11.8	0.21	14	~0.4

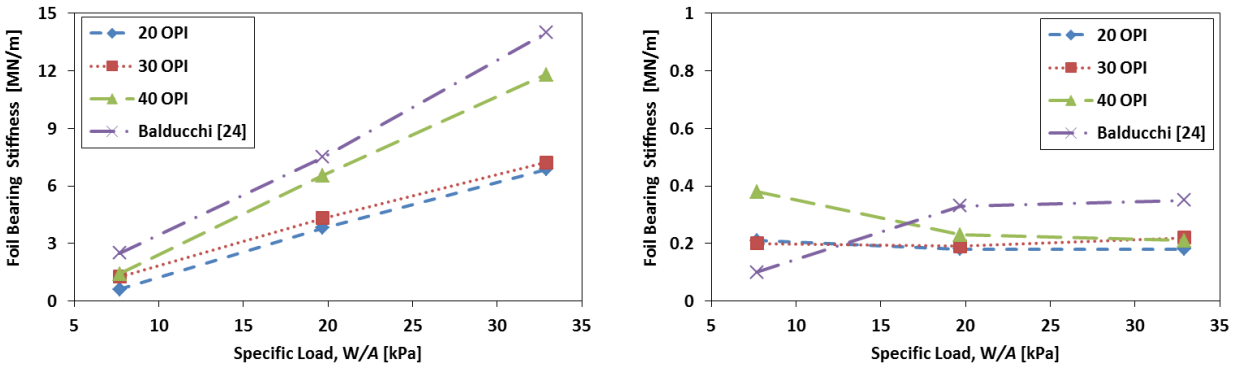

(a) Stiffness versus applied load

(b) Loss factor (γ) versus applied load

Figure 23. Average foil bearing stiffness and material loss factor versus applied specific load (*W/A*) for four thrust foil bearings.

BREAKAWAY TORQUE FOR COATED AND UNCOATED METAL MESH FOIL THRUST BEARINGS

During start-up and shut-down events, foil thrust bearings experience contact between the runner and the foils. Characterizing the torque required to separate the shaft from the bearing during start-up is crucial for selecting a proper motor, or driver.

Figure 24 displays a photograph of the torque measurement apparatus on the foil thrust bearing rig. It consists of a strain gauge load cell attached to the back of the load shaft via a rod end bearing and threaded torque arm. The threaded (10-32 UNF) rod fits into an 1/8th" NPT cross connection that screws to the back of the load shaft. Because the porous bushings float the shaft (no friction), the product of the lever arm length (40.64 mm) and the measured static load determines the bearing drag torque.

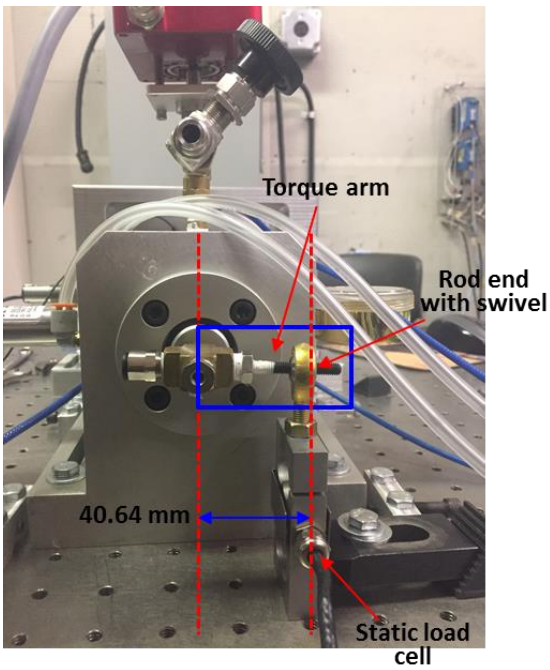

Figure 24. Depiction of drag torque measuring system with strain gauge load cell and a lever arm affixed to the load shaft.

A precise (±0.01) digital torque screwdriver calibrates the torque measuring system (static load · lever arm), ensuring its accuracy, and verifying the proper length of the lever arm (l = 40.64 mm).

After calibrating the torque measuring system, several tests characterize the *break-away* torque for a MMFTB with two top foils, one coated with Parylene N® and the other with a plains 316 SS surface. Note this torque, when applied, opposes the contact shear stresses between the bearing and thrust collar. The *break-away* torque is strictly a dry-friction (dynamic) torque and does not correspond to the torque at which the rotor lifts from its bearing. This *break-away* torque must be overcome by the drive rotor to initiate operation with dry-friction sliding (contact).

For the uncoated bearing, the applied specific axial load ranges from 7.7-32.9 kPa, while the coated bearing is only tested at the two lowest specific loads (7.7 and 13.2 kPa) to ensure the integrity of the Parylene N coating. Following Norsworthy [26], a friction factor for the TFB is construed as

$$f = \frac{T}{WR_{mid}} \tag{11}$$

where T is the *break-away* torque, W is the applied static load and R_{mid} a radius to the pad center (R = 0.0381 m).

Figure 25 displays the dry-sliding friction factor versus specific load for a MMFTB with three sheets of 40 OPI mesh and with either a coated top foil or a plain, uncoated foil. Each data point in Figure 25 represents the average of 5 individual trials and, as noted in the figure, the uncertainty for the measurements is 0.016 and refers to the largest standard deviation encountered for a set of 5 measurements. The torque required to break the initial friction between the top foil and the runner is rather large (T~0.44 N.m), even for small loads (W/A = 7.7 kPa). For the largest applied load, the torque necessary to break the surfaces' contact approaches T=2.25 N.m, two fold or more than 1.1 N/m, the max torque the drive motor can apply. The Parylene coating does provide slightly less friction, but overall, the MMFTB requires a large torque to break the static friction.

Although not specifically addressed by Stahl, results in [15] show that for a lightly loaded BFTB (W/A ~ 9 kPa), the drag toque during start-up and shut down torque exceeds 0.23 N.m.

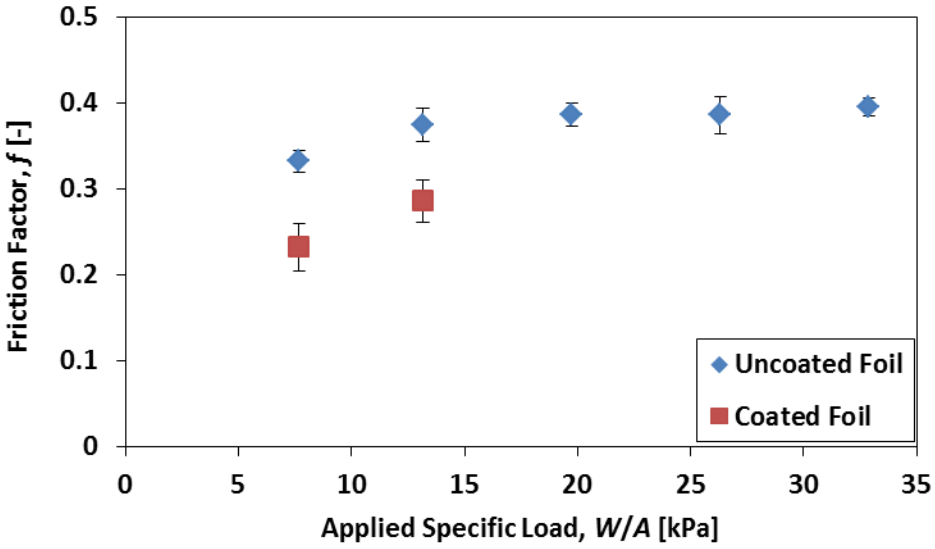

Figure 25. Sliding friction factor vs. specific load for a MMFTB: coated top foil and uncoated top foil.

Figure 26 displays the post-test condition of the coated and uncoated top foils after the break-away torque measurements. As the uncoated foil was subject to larger loads, and more cycles, the wear on its surface is more visible, being evenly distributed over the 6 pads as well as from the pads inner to outer

radii. The coated foil also evidences wear, showing areas where the Parylene coating has abraded. The uncoated foil has wear on both the step and land areas of each pad, while the coated bearing only shows wear on the step areas, indicating that only the steps are in solid contact with the thrust collar and with $W/A < 20$ kPa.

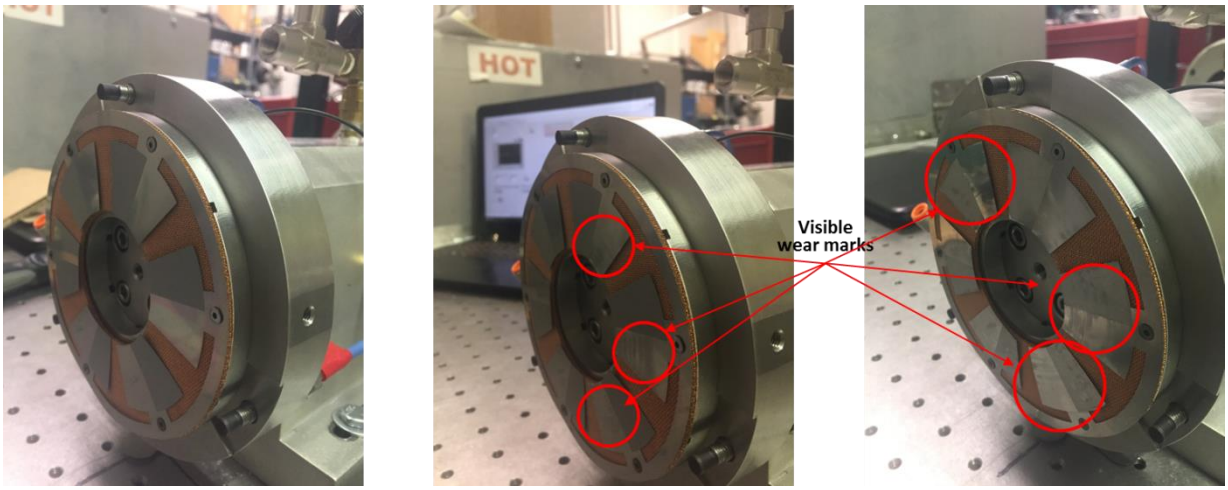

(a) MMTFB prior to testing (b) Coated MMTFB post testing (c) Uncoated MMTFB post testing

Figure 26. Photographs of MMFTBs before and after break-away torque tests.

With an adequate knowledge of the MMFTB's structure performance (static load versus deflection) and frictional characteristics, the bearing is ready for tests with rotor speed. In future tests, the Rayleigh step foil will be instrumented with three thermocouples to measure the temperatures of the different bearing pads.

Future work intends to characterize the performance of the MMFTB and compare it to that of an identical sized BFTB.

CLOSURE

The report describes the design and construction of a test rig for evaluation of thrust foil bearings. The test rig, consisting of an aerostatic loading plenum, load shaft, thrust runner and test bearing facilitates the measurement of: foil thrust bearing static load versus deflection behavior, static break-away torque, structural force coefficients, lift-off speed, bearing pad temperatures and bearing load capacity. In addition to the functionality of the test rig, the above presents the design and manufacturing of a novel metal mesh foil thrust bearing. A MMFTB bearing consists of one or more mesh layers and a top foil making six-pads, each with a Rayleigh-step.

Load versus deflection tests with the prototype MMFTB show that the MMFTB has a similar structural stiffness to a BFTB from the archival literature [15]. In addition to static load tests, single frequency dynamic load tests reveal that the MMFTB has a material loss factor $\gamma \sim 0.2$ that is largely unaffected by excitation frequency or applied load. The metal mesh structural dynamic stiffness (K) increases with applied load and also with the mesh mass ratio (or openings per inch). Static break-away torque measurements show that the Parylene® coating slightly reduces the coefficient of friction (f~0.2) between the MMFTB and the thrust collar.

Future work intends to characterize the drag torque, pad temperature rise and load capacity of this bearing type under increasing static loads and rotor speeds up to 40 krpm. An existing numerical tool for the prediction of BFTB performance will be extended to model MMFTBs and the thermal energy transport equation will be included to account for temperature effects in the thin film, thrust collar, and top foils.

REFERENCES

[1] Agrawal, G. L., 1997, "Foil Air/Gas Bearing Technology – an Overview," ASME Paper No. 97-GT-347.

[2] Heshmat, H., Walowit, J.A. and Pinkus, O., 1983, "Analysis of Gas Lubricated Compliant Thrust Bearings," ASME J. Tirb., **105**, pp. 638-646.

[3] Heshmat, H., "Analysis of Compliant Foil Bearings with Spatially Variable Stiffness, AIAA/SAE/ASME/ASEE 27th Joint Propulsion Conference, AIAA-91-2102.

[4] Heshmat, C.A., Xu, D.S. and Heshmat, H., 2000, "Analysis of Gas Lubricated Foil Thrust Bearings Using Coupled Finite Element and Finite Difference Methods," ASME J. Trib., **122**, pp. 199-204.

[5] Hryniewicz, P., Locke, D. H. and Heshmat, H., 2003, "New-Generation Development Rigs for Testing High-Speed Air-Lubricated Thrust Bearings," Trib. Trans., **46**(4), pp. 556- 559.

[6] Iordanoff, I., 1998, "Maximum Load Capacity Profiles for Gas Thrust Bearings Working Under High Compressibility Number Conditions", ASME J. Trib, **120**, pp. 571- 576.

[7] Iordanoff, I., 1999, "Analysis of an Aerodynamic Compliant Foil Thrust Bearing: Method for a Rapid Design," ASME J. Trib, **121**, pp. 816- 821.

[8] Gu, A. L. and Nadjafi, R.H., 1993, "Foil Thrust Bearing With Varying Radial and Circumferential Stiffness," US Patent 5248205.

[9] Heshmat, H., 1999, "High Load Capacity Compliant Foil Hydrodynamic Thrust Bearing," US Patent 5961217.

[10] Bruckner, R. J., 2004, "Simulation and Modeling of the Hydrodynamic, Thermal and Structural Behavior of Foil Thrust Bearings," PhD thesis, Case Western Reserve University, Cleveland, OH.

[11] Dykas, B., 2006, "Factors Influencing the Performance of Foil Gas Thrust Bearings for Oil Free Turbomachinery Applications", PhD Dissertation, Case Western Reserve University, Cleveland, OH.

[12] Dykas, B., Bruckner. R., DellaCorte, C. and Edmonds, B., 2008, "Design, Fabrication, and Performance of Foil Gas Thrust Bearings for Microturbomachinery Applications", NASA/TM-2008-215062, NASA Glenn Research Center, Cleveland, OH.

[13] Dykas, B., Bruckner, R., DellaCorte, C., Edmonds, B. and Prahl, J., 2009, "Design, Fabrication, and Performance of Foil Gas Thrust Bearings for Microturbomachinery Applications," ASME J. Eng. Gas Turbines Power, **131**, pp. 1-8.

[14] Dickman, J.R., 2010, "An Investigation of Gas Foil Thrust Bearing Performance and its Influencing Factors," MS Thesis, Case Western Reserve University, Cleveland, OH.

[15] Stahl, B.J., 2012, "Thermal Stability and Performance of Foil Thrust Bearings," MS Thesis, Case Western Reserve University, Cleveland, OH.

[16] San Andrés, L., Ryu, K. and Diemer, P., 2015, "Prediction of Gas Thrust Foil Bearing Performance for Oil-Free Automotive Turbochargers," ASME J. Eng. Gas Turbines Power, **137**, pp. 1-10.

[17] Ryu, K. and Ashton, Z., 2016, "Bump-Type Foil Bearings and Flexure Pivot Tilting Pad Bearings for Oil-Free Automotive Turbochargers: Highlights in Rotordynamic Performance," ASME J. Eng. Gas Turbines Power, **138**, pp. 1-10.

[18] Choe, B. S., Kim, T.H., Kim, C.H. and Lee, Y.B., 2015, "Rotordynamic Behavior of 225 kW (300 HP) Class PMS Motor-Generator System Supported by Gas Foil Bearings," ASME J. Eng. Gas Turbines Power, **137**, pp. 1-8.

[19] Chirathadam, T. A., and San Andrés, L., 2012, "A Metal Mesh Foil Bearing and a Bump Type Foil Bearing: Comparison of Performance for Two Similar Size Gas Bearings," ASME J. Eng. Gas Turbines Power, 134, pp. 10250.

[20] Alkhateeb, E.M., 2002, "Design, Modeling and Experimental Investigation of Mesh Vibration Dampers," Ph.D. Dissertation, Department of Mechanical Engineering, Texas A&M University.

[21] Chirathadam, T.A., 2012, "Metal Mesh Foil Bearings: Prediction and Measurement of Static and Dynamic Performance Characteristics," Ph.D. Dissertation, Texas A&M University, College Station, TX.

[22] Hashimoto, H. and Ochiai, M., 2007, "Theoretical Analysis and Optimum Design of High Speed Gas Film Thrust Bearings (Static and Dynamic Characteristic Analysis with Experimental Verifications)," J. Advanced Mechanical Design, **1** (1), pp. 1-11.
[23] Lee, D. and Kim, D., 2011, "Three-Dimensional Thermohydrodynamic Analyses of Rayleigh Step Air Foil Thrust Bearing with Radially Arranged Bump Foils," Trib. Trans., **vol. 54**, pp. 432-448.
[24] Balducchi, F., Arghir, M. and Gauthier, R., 2015, "Experimental Analysis of the Dynamic Characteristics of a Foil Thrust Bearing," ASME J. Trib., **vol. 37**, pp. 1-9.
[25] Burrows, C. R., Sayed-Esfahani, R., and Stanway, R., 1981, "Comparison of Multifrequency Techniques for Measuring the Dynamics of Squeeze-Film Bearings," ASME J. Lubr. Technol., **vol. 103**, pp. 137–143.
[26] Norsworthy, J.D., 2014, "Measurement of Drag Torque, Lift Off Speed, and Identification of Frequency Dependent Stiffness and Damping Coefficients of a Shimmed Bump-Type Foil Bearing," MS Thesis, Mechanical Engineering Dept., Texas A&M University, College Station, TX.
[27] Cable. T.A. and San Andrés, 2016, "Structural Force Coefficients from Metal Mesh Pads for a Foil Bearing," Annual Progress Report to Turbomachinery Research Consortium, TRC-B&C-02-2016, pp. 1-49.